Multiplexed identification of RAS paralog imbalance as a driver of lung cancer growth

Rui Tang[1*], Emily G. Shuldiner[2*], Marcus Kelly[3,4], Christopher W. Murray[3], Jess D. Hebert[1], Laura Andrejka[1], Min K. Tsai[1,3], Hongchen Cai[1], Yao-Cheng Li[5], Geoffrey M. Wahl[5], Peter K. Jackson[3,4], Dmitri A. Petrov[2,3], and Monte M. Winslow[1,3,6#]

[1] Department of Genetics, Stanford University School of Medicine, Stanford, CA, USA

[2] Department of Biology, Stanford University, Stanford, CA, USA

[3] Cancer Biology Program, Stanford University School of Medicine, Stanford, CA, USA

[4] Baxter Laboratories, Stanford University School of Medicine, Stanford, CA, USA

[5] Gene Expression Laboratory, The Salk Institute for Biological Studies, La Jolla, CA, USA

[6] Department of Pathology, Stanford University School of Medicine, Stanford, CA, USA

[*] These authors contributed equally

[#] Corresponding author: Monte M. Winslow: mwinslow@stanford.edu

ABSTRACT

Oncogenic *KRAS* mutations occur in approximately 30% of human lung adenocarcinoma. Despite tremendous effort over the past several decades, oncogenic KRAS-driven lung cancer remains difficult to treat, and our understanding of the positive and negative regulators of RAS signaling is incomplete. To uncover and corroborate the functional impact of diverse KRAS-interacting proteins on lung cancer growth *in vivo*, we integrate somatic CRISPR/Cas9-based genome editing in genetically engineered mouse models with tumor barcoding and high-throughput barcode sequencing (Tuba-seq). Through a series of *in vivo* CRISPR/Cas9 screens, we identified HRAS and NRAS as key suppressors of $KRAS^{G12D}$-driven lung tumor growth *in vivo* and confirmed these effects in oncogenic KRAS-driven human lung cancer cell lines. Mechanistically, we find that these RAS paralogs interact with oncogenic $KRAS^{G12D}$, suppress $KRAS^{G12D}$-$KRAS^{G12D}$ interaction, and reduce downstream ERK signaling. Patient-derived mutations $HRAS^{T50M}$ and $HRAS^{R123C}$ partially abolished this effect. Comparison of the tumor-suppressive effects of HRAS and NRAS in $KRAS^{G12D}$- and $BRAF^{V600E}$-driven lung cancer models confirmed that these RAS paralogs are specific suppressors of oncogenic KRAS-driven lung cancer *in vivo*. Our study outlines a technological avenue to specifically uncover positive and negative regulators of oncogenic KRAS-driven cancer in a multiplexed manner and highlights the role of RAS paralog imbalance in oncogenic KRAS-driven cancers.

50 **INTRODUCTION**

51 The RAS gene family, which consists of *KRAS*, *HRAS* and *NRAS*, is the most frequently
52 mutated across all cancers, and *KRAS* mutations occur in approximately 30% of all lung
53 adenocarcinomas (1-3). RAS proteins are small GTPases that switch between a GTP-bound
54 active state and GDP-bound inactive state in response to upstream growth signaling (4). Active
55 RAS proteins drive downstream signaling such as MAPK and PI3K pathways, thereby
56 promoting cell growth. In cancer, hotspot oncogenic mutations in codons 12, 13, and 61 reduce
57 GTP hydrolysis and increase the fraction of RAS proteins in the GTP-bound state, which results
58 in constitutive activation and significant changes in RAS protein-protein interactions (5,6). These
59 changes result in hyper-activation of RAS effector pathways, driving cellular transformation and
60 tumorigenesis (7,8). Oncogenic KRAS therefore represents a critical target for therapeutic
61 intervention in lung adenocarcinoma. However, despite tremendous effort, the development of
62 targeted therapies for oncogenic KRAS-driven tumors has proven challenging (9). RAS-
63 interacting proteins include many important regulators and effectors that remain poorly
64 understood in the context of oncogenic KRAS-driven lung cancer, and a better understanding of
65 these interactions could enable the identification of indirect therapeutic strategies to counteract
66 oncogenic KRAS activity (10).

67 Much of our understanding of RAS signaling has stemmed from diverse cellular and cell-
68 free systems (11-13). Recent advances have led to the mapping of KRAS protein-protein
69 interaction networks, as well as identified synthetic lethal interactions with oncogenic KRAS in
70 human cell lines (14-16). Nevertheless, it is still difficult to relate these *in vitro* findings to
71 human cancer. Genetically engineered mouse models of oncogenic KRAS-driven cancer
72 uniquely recapitulate autochthonous tumor growth and have contributed greatly to our

73 understanding of KRAS signaling, but the development and use of such models has traditionally
74 been insufficiently scalable to model the diverse genetics of human cancer. The ability to
75 multiplexed identification of novel key components in RAS signaling in mouse lung cancer
76 models would thus greatly enhance our understanding of RAS biology and aid in the
77 development of pharmacological strategies to counteract hyperactivated KRAS.

78 To enable the analysis of modifiers of oncogenic KRAS-driven growth, we recently
79 integrated somatic CRISPR/Cas9-based genome editing with tumor barcoding and high-
80 throughput barcode sequencing (Tuba-seq) (17-19). This approach allows precise quantification
81 of the impact of inactivating panels of genes of interest in promoting lung tumor initiation and
82 growth in a multiplexed manner. By employing Tuba-seq to assess the functions of KRAS-
83 interacting proteins captured by unbiased affinity purification/mass spectrometry (AP/MS), we
84 show that wild-type HRAS and NRAS suppress the growth of oncogenic KRAS-driven lung
85 adenocarcinoma. Competitive binding between oncogenic KRAS and wild-type HRAS
86 diminishes KRAS-KRAS interaction that is required for RAS effector recruitment and
87 consequently suppresses downstream signaling. *In vivo* screening across multiple oncogenic
88 contexts revealed that HRAS and NRAS specifically suppress oncogenic KRAS-driven tumor
89 growth. Our study reveals RAS paralog imbalance as a driver of oncogenic KRAS-driven lung
90 cancer.

91

92 **RESULTS**

93

94 **Selection of candidate KRAS-interacting proteins to assess *in vivo***

95 Oncogenic KRAS represents a key node downstream of growth factor-induced signaling,
96 and oncogenic KRAS is sufficient to initiate tumor growth in several different tissues (20,21).
97 Genetic and proteomic mapping have revealed that KRAS interacts with a large network of
98 proteins outside of its canonical effectors and regulators (14,15). To identify putative KRAS-
99 interacting proteins that could affect oncogenic KRAS-driven lung tumor growth *in vivo*, we
100 integrated proteomics data from AP/MS studies with gene expression data from cancer cells
101 from autochthonous mouse models **(Figure 1a)**. We prioritized a list of candidate genes
102 according to the probability of their protein products binding to KRAS, their abundance of
103 homolog mRNA in mouse models of oncogenic $KRAS^{G12D}$-driven lung cancer, and the
104 probability of their protein products binding to other small GTPases **(Figure 1b-c)** (14,22). We
105 selected 13 proteins that represent diverse aspects of RAS biology, including RAS paralogs
106 (HRAS, NRAS), RAS regulators (RASGRF2, RAP1GDS1) (23,24), a RAS modifier (FNTA)
107 (25), and RAS effectors (RAF1, RGL2) (14,26), as well as other proteins whose functions in
108 RAS signaling are understudied. Interestingly, some of these proteins bound preferentially to
109 either GTP- or GDP-bound KRAS, while others seemed to interact with KRAS independent of
110 its nucleotide state **(Figure 1c)**.
111

112 **Identification of KRAS-interacting proteins that impact lung tumor growth *in vivo***

113 Given that KRAS-interacting proteins could have either positive or negative effects on
114 signaling and tumor growth, we first assessed whether Tuba-seq is capable of detecting gene-
115 targeting events that have deleterious effects on tumor fitness. We initiated tumors in $Kras^{LSL-}$
116 $^{G12D/+}$;$Rosa26^{LSL-tdTomato}$;$H11^{LSL-Cas9}$ (*KT;*$H11^{LSL-Cas9}$) and control *KT* mice with a pool of
117 barcoded Lenti-sgRNA/Cre vectors encoding sgRNAs targeting two essential genes (*Pcna* and

118 *Rps19*) and a known tumor suppressor (*Apc*), in addition to several inert sgRNAs (Lenti-
119 sgEssential/Cre; **Figure S1a**). After 12 weeks of tumor growth, we performed Tuba-seq on bulk
120 tumor-bearing lungs and quantified the number and size of tumors initiated with each Lenti-
121 sgRNA/Cre vector (**Figure S1b**). By incorporating measures of tumor number and tumor size
122 across each tumor size distribution, we could confidently identify genetic deficiencies that
123 reduced tumor fitness (**Figure S1c-g and Methods**).

124 To quantify the impact of inactivating our panel of KRAS-interacting proteins on
125 oncogenic $KRAS^{G12D}$-driven lung tumor growth *in vivo*, we generated a pool of barcoded Lenti-
126 sgRNA/Cre vectors targeting the genes that encode each protein, as well as sg*Inert* control
127 vectors (Lenti-sg*KrasIP/Cre*; **Figure 1d**). Given the importance of farnesylation in KRAS
128 localization and signaling, we included a vector targeting *Fnta* as a control dependency (27,28).
129 We initiated tumors with the Lenti-sg*KrasIP/Cre* pool in *KT;H11*$^{LSL\text{-}Cas9}$ and *KT* mice and
130 calculated metrics of tumor size and number after 12 weeks of tumor growth (**Figure 1e**). To our
131 surprise, inactivation of the *Kras* paralogs *Hras* and *Nras* had the most dramatic effect on tumor
132 growth. Inactivation of *Cand1* also increased tumor size, while deficiencies in *Nme2*, *Rapgds1*,
133 and *Aldh1a* decreased tumor size (**Figure 1f**). Several other genes decreased tumor number
134 and/or size suggesting reduced cancer cell fitness (**Figure 1f** and **S2a-c**). Consistent with our
135 findings using the Lenti-sgEssential/Cre pool, inactivation of *Pcna* and *Fnta* dramatically
136 reduced tumor number (**Figure 1f** and **S2d**).

137 Given the fundamental importance of the p53 tumor suppressor in oncogenic KRAS-
138 driven lung cancer, as well as previous data suggesting crosstalk between RAS and p53
139 signaling(18,29), we determined whether p53 deficiency dramatically changes the impact of
140 inactivating KRAS-interacting proteins on tumor growth. We initiated tumors with the Lenti-

141 sg*KrasIP/Cre* pool in *Kras*$^{LSL\text{-}G12D/+}$;*Trp53*$^{flox/flox}$;*Rosa26*$^{LSL\text{-}tdTom}$;*H11*$^{LSL\text{-}tdTom}$ (*KPT;H11*$^{LSL\text{-}Cas9}$)
142 mice and performed Tuba-seq after 12 weeks of tumor growth. The effects of inactivating each
143 gene encoding a KRAS-interacting protein on tumor size, tumor number, and overall tumor
144 burden were generally consistent between the p53-proficient and -deficient settings (**Figure 1g,**
145 **Figure S2e-h**). Notably, the inactivation of either *Hras* or *Nras* also significantly increased
146 growth of p53-deficient tumors (**Figure S2e).** Collectively, these results suggested that HRAS
147 and NRAS have the strongest tumor-suppressive functions within *in vivo* models of oncogenic
148 KRAS-driven lung cancer, while the other four KRAS-interacting proteins, including CAND1,
149 ALDH1A, FNTA, and NME2, have consistent positive or negative effects on tumor growth
150 (**Figure S2e-h)**.
151

152 **Validation of HRAS and NRAS as suppressors of oncogenic KRAS-driven lung tumor**
153 **growth**

154 To further validate the impact of inactivating the six top candidate genes (*Hras, Nras,*
155 *Cand1, Aldh1a, Fnta, and Nme2*) on oncogenic KRAS-driven tumor growth *in vivo* and confirm
156 that these results are driven by on-target effects, we generated and barcoded three Lenti-
157 sgRNA/Cre vectors targeting each gene. To put the impact of *Hras* and *Nras* inactivation on lung
158 tumor growth in context, we included vectors targeting three established tumor suppressors
159 (*Lkb1, Rbm10*, and *Rb1*) in this pool (Lenti-sgValidation/Cre; **Figure 2a**) (17,19,30). We
160 initiated tumors with the Lenti-sgValidation/Cre pool in *KT;H11*$^{LSL\text{-}Cas9}$ and *KT* mice and
161 assessed metrics of tumor initiation and growth 12 weeks after tumor initiation (**Figure 2b-c,**
162 **Figure S3**). Targeting *Fnta* with all three sgRNAs consistently reduced growth fitness while the
163 impact of inactivating *Aldh1a* and *Nme2* was more variable (**Figure 2d, Figure S3**). Most

164 importantly, all three sgRNAs targeting *Hras* and all three sgRNAs targeting *Nras* significantly
165 increased tumor growth (**Figure 2d-e, Figure S3**). Notably, the impact of *Hras* inactivation was
166 similar in magnitude to that of *Rb1* and *Rbm10* tumor suppressors (**Figure 2d, Figure S3**). These
167 results suggest a potentially pivotal role for wild-type HRAS and NRAS in constraining
168 oncogenic KRAS-driven lung tumor growth *in vivo*.

169 In addition, we validated the tumor-suppressive function of HRAS and NRAS in
170 oncogenic KRAS-driven lung tumor growth by initiating tumors in *KT;H11*$^{LSL\text{-}Cas9}$ mice with
171 individual sg*Inert*-, sg*Hras*- and sg*Nras*-encoding Lenti-sgRNA/Cre vectors (**Figure 2f**).
172 Inactivation of either *Hras* or *Nras* increased tumor growth as assessed by direct fluorescence
173 and histology (**Figure 2g-i**). Collectively, these results suggest that RAS paralogs constrain the
174 growth of oncogenic KRAS-driven lung cancer growth.

175

176 **HRAS and NRAS can be growth-suppressive in human lung cancer cells**

177 To assess the relevance of HRAS and NRAS as tumor suppressors in human lung cancer,
178 we tested the function of HRAS and NRAS in oncogenic KRAS-driven human adenocarcinoma
179 cell lines. Previous genome-scale CRISPR/Cas9 screens revealed a variable effect of inactivating
180 these genes on cancer cell line growth under standard culture conditions (**Figure S4a)**.
181 Interestingly, HRAS and NRAS suppressed the growth of oncogenic KRAS^{G12S}-driven A549
182 cells and had a greater effect on the growth of several oncogenic KRAS-driven lung cancer cell
183 lines when grown in 3D culture conditions (**Figure S4b-c**) (14,16). To further assess the
184 functions of HRAS and NRAS in oncogenic KRAS-driven human adenocarcinoma cell lines, we
185 performed gain and loss of function studies on H23 (KRAS^{G12C}) and H727 (KRAS^{G12V}) cells.
186 We inactivated *HRAS* and *NRAS* using CRISPR/Cas9 and generated variants with doxycycline-

187 inducible wild-type *Hras* re-expression. Inactivation of *Hras* or *Nras* in oncogenic KRAS-driven
188 cells increased proliferation when cells were grown with limited serum and increased clonal
189 growth potential when cells were grown in anchorage-independent conditions (**Figure 3a, c, d**).
190 Conversely, re-expression of HRAS in these *Hras*-null cells impaired proliferation and clonal
191 growth (**Figure 3b, e, f**). H23 cells with inactivated *Hras* or *Nras* also formed larger and more
192 proliferative tumors after intravenous and subcutaneous transplantation (**Figure 3g-k, Figure**
193 **S5**). These results demonstrate that wild-type HRAS and NRAS can also function as tumor
194 suppressors in oncogenic KRAS-driven human lung cancer cells *in vitro* and *in vivo*. This
195 consistency between human cell culture and autochthonous mouse models further suggests that
196 HRAS and NRAS are tumor suppressors in oncogenic KRAS-driven lung adenocarcinoma.
197

198 **Inactivation of RAS paralogs increases signaling downstream of oncogenic KRAS**

199 Wild-type KRAS has been shown to be tumor-suppressive in multiple experimental
200 models of oncogenic KRAS-driven cancer, likely due to its ability to directly bind and
201 antagonize oncogenic KRAS (31-33). We have demonstrated that wild-type HRAS and NRAS
202 suppress oncogenic $KRAS^{G12D}$-driven lung cancer growth *in vivo*. Thus, to further explore the
203 molecular mechanism driving this effect, we assessed whether HRAS and NRAS alter signaling
204 downstream of oncogenic KRAS. We initially performed pERK immunohistochemistry on lung
205 tumors initiated with sg*Inert*, sg*Hras* or sg*Nras* containing Lenti-sgRNA/Cre vectors in
206 *KT;H11*$^{LSL\text{-}Cas9}$ mice. Inactivation of HRAS or NRAS increased the number of pERK-positive
207 cells in $KRAS^{G12D}$-driven lung cancer (**Figure 4a**). Subcutaneous tumors from transplanted H23
208 cells with inactivated *HRAS* or *NRAS* also contains more pERK-positive cells comparing to
209 tumors from transplanted wildtype (sg*SAFE*) H23 cells (**Figure 4b**). In addition, sorted cancer

210 cells from *KT;H11*$^{LSL\text{-}Cas9}$ mice with lung tumors initiated with Lenti-sg*Hras*/Cre also expressed
211 more pERK comparing to those from tumors initiated with Lenti-sg*Inert*/Cre (**Figure 4c**). At last,
212 inactivation of either *Hras(HRAS)* or *Nras(NRAS)* in mouse or human oncogenic KRAS-driven
213 cell lines increased ERK phosphorylation (**Figure 4d-e**). Conversely, re-expression of wild-type
214 HRAS in HRAS-null H23 human lung cancer cells reduced ERK phosphorylation (**Figure 4g**).
215 Previous publications have shown that inactivating wild-type KRAS increases sensitivity to
216 MEK inhibitors. Consistent with these studies of wild-type KRAS, we found that inactivation of
217 *HRAS* in H23 cells increases sensitivity to the MEK inhibitor trametinib while re-expression of
218 HRAS made cells more resistant (**Figure 4f, h**). These data suggest that inactivation of *HRAS* or
219 *NRAS* hyper-activates MAPK signaling in KRAS mutant cancer cells (34-36).
220

221 **RAS paralogs competitively suppress KRAS^{G12D}-KRAS^{G12D} interaction**

222 RAS proteins interact with themselves and forms functional clusters on membrane to efficiently
223 recruit downstream effectors (37-39). Homodimers of all RAS paralogs have been reported (40-
224 42). However, there was relatively little evidence supporting the existence of RAS heterodimers
225 and their biological functions. AP/MS data suggested that both HRAS and NRAS strongly
226 interacted with KRAS, supporting the existence of heterotypic RAS-RAS interactions (**Figure**
227 **5a**). To assess the ability of RAS paralogs to bind oncogenic KRAS^{G12D}, we adapted a recently
228 published luminescent reporter system (ReBiL2.0 system), which relies on luciferase
229 complementation to quantify RAS-RAS interactions in living cells (43). Through expression of
230 wild-type KRAS, HRAS, or NRAS paralogs in KRAS^{G12D}-KRAS^{G12D} reporter cells or control
231 reporter cells, we found that all wild-type RAS paralogs are able to disrupt KRAS^{G12D}-
232 KRAS^{G12D} interaction **(Figure 5b)**. These findings are consistent with a model in which wild-

233 type RAS paralogs competitively bind to oncogenic KRAS and thus suppress $KRAS^{G12D}$-
234 $KRAS^{G12D}$ interaction and downstream signaling.
235
236 **Patient-derived $HRAS^{T50M}$ and $HRAS^{R123C}$ mutations impair interaction of HRAS with**
237 **oncogenic KRAS and abrogate its tumor suppressive function**
238 Given that our findings suggest that the tumor-suppressive function of wild-type HRAS is
239 mediated by competitive binding to oncogenic KRAS, we hypothesized that there could be
240 *HRAS* mutations in lung adenocarcinoma samples with oncogenic *KRAS* that confer a fitness
241 benefit by impairing interaction with oncogenic KRAS. To evaluate this possibility, we analyzed
242 data from The Cancer Genome Atlas (TCGA) and AACR's Genomics Evidence Neoplasia
243 Information Exchange (Project GENIE). As expected, mutations in *HRAS* were rare and the
244 majority were oncogenic mutations (occurring in codons 12, 13 or 61) in samples lacking
245 oncogenic *KRAS*. We did, however, identify multiple rare non-oncogenic *HRAS* mutations that
246 occurred in samples with oncogenic KRAS. To test our hypothesis that some or all of these
247 mutations lack the ability to interact with oncogenic KRAS, we used the ReBiL2.0 system to
248 measure the ability of four of these *HRAS* mutations and a known dimerization-deficient control
249 (Y64A) to reduce $KRAS^{G12D}$-$KRAS^{G12D}$ interaction (41). This assay identified two mutations,
250 T50M and R123C, that are unable to disrupt $KRAS^{G12D}$-$KRAS^{G12D}$ binding to an extent similar
251 to Y64A (**Figure 5c**). Previous publications have shown that HRAS has low affinity binding to
252 RAF proteins and other RAS effectors and thus functions as a sterile end in RAS-RAF-MEK
253 signaling. Furthermore, by re-analyzing a previously published AP-MS dataset, we found that
254 GTP-bound HRAS is more similar in its affinity for RAS effectors to GDP-bound KRAS and
255 NRAS than to their GTP-bound forms, suggesting a lack of oncogenic signaling downstream of

256 HRAS in lung adenocarcinoma (**Figure 5d**) (14). To test our hypothesis that the disruption of
257 $KRAS^{G12D}$-$KRAS^{G12D}$ interaction by HRAS suppresses downstream oncogenic signaling, we re-
258 expressed wild-type HRAS, dimerization deficient $HRAS^{Y64A}$, or the two novel patient-derived
259 $HRAS^{T50M}$ and $HRAS^{R123C}$ in *HRAS*-null lung cancer cells. Re-expression of wild-type HRAS,
260 but not any of these three known or novel mutants suppressed ERK phosphorylation and cell
261 proliferation (**Figure 5e-f**). These results further suggest that RAS paralog imbalance fine tunes
262 oncogenic KRAS signaling via disrupting oncogenic KRAS-wildtype RAS paralog interaction
263 and thus is a driver of lung cancer growth.
264

265 **HRAS and NRAS are specific suppressors of oncogenic KRAS-driven lung cancer growth**

266 Our *in vivo* data demonstrate that HRAS and NRAS function as tumor suppressors, and
267 our cell culture results suggest that these effects may be mediated by interaction of these RAS
268 paralogs with oncogenic KRAS. If the tumor-suppressive mechanism by which HRAS and
269 NRAS act requires interaction with oncogenic KRAS, then these genes should not be tumor
270 suppressors in a model of lung adenocarcinoma in which activation of the RAS signaling
271 pathway occurs downstream of KRAS. To test this prediction of our model directly in
272 autochthonous tumors, we initiated tumors with a sub-pool of barcoded lenti-sgRNA/Cre vectors
273 (Lenti-sgMultiGEMM/Cre) in mouse models of $KRAS^{G12D}$-driven and $BRAF^{V618E}$ (the mouse
274 equivalent of $BRAF^{V600E}$)-driven lung cancer (44). In addition to vectors targeting *Hras* and
275 *Nras*, this pool included vectors targeting several known tumor suppressors (*Apc, Rbm10*, and
276 *Cdkn2a*), other KRAS-interacting proteins (*Aldh1a, Cand1, Nme2*), and control vectors (**Figure**
277 **6a**). We initiated tumors with the Lenti-sgMultiGEMM/Cre pool in *KT*, *KT;H11*$^{LSL\text{-}Cas9}$ and
278 *Braf*$^{CA/+}$*T;H11*$^{LSL\text{-}Cas9}$ mice and assessed tumor initiation and growth 15 weeks after tumor

279 initiation (**Figure 6b**). Consistent with previously published results, delivery of identical
280 lentiviral titers resulted in visibly increased tumor mass and greater lung weight in
281 *Braf*$^{CA/+}$*T;H11*$^{LSL\text{-}Cas9}$ mice than in *KT;H11*$^{LSL\text{-}Cas9}$ mice (**Figure 6c-d**). Comparison of the
282 distribution of sgInert tumor sizes in the two models using Tuba-seq allows us to directly
283 compare the effects of the *Braf*^{V618E} and *Kras*^{G12D} oncogenes on tumor growth. Braf^{V618E} tumors
284 are larger than Kras^{G12D} tumors (median size of ~3500 cells vs ~1000 cells), but the two
285 distributions have similar right tails and maximum tumor sizes, suggesting that the observed
286 increase in tumor burden is driven by a shift in density towards larger tumors of relatively
287 uniform size, rather than by the emergence of a small number of very large tumors (**Figure 6e-f**).
288 Importantly, while inactivation of *Hras* or *Nras* increased the growth of oncogenic KRAS-driven
289 lung tumors, inactivation of *Hras* or *Nras* had no impact on the growth of oncogenic BRAF-
290 driven lung cancer (**Figure 6g**). Thus, these data further support our model in which HRAS and
291 NRAS function as specific suppressors of oncogenic KRAS-driven tumor growth, likely through
292 direct interaction with oncogenic KRAS but not RAS effectors. The pathways that suppress
293 oncogenic BRAF-driven lung cancer are less well-studied as compared to those that impact
294 oncogenic KRAS-driven lung cancer. Thus, the effects of *Apc*, *Cdkn2a*, and *Rbm10* inactivation
295 not only represent controls for the success of this *in vivo* counter-screen but also identified
296 instances of oncogene-tumor suppressor epistasis. For example, inactivation of *Apc* has a
297 significantly greater effect on tumor growth in BRAF-driven lung cancer than in KRAS-driven
298 lung cancer, whereas the effect of inactivation of *Rbm10* is diminished (**Figure 6h**). Finally,
299 inactivation of *Nme2*, *Fnta*, and *Aldh1a* reduced tumor initiation and growth in both oncogenic
300 KRAS-driven and oncogenic BRAF-driven lung cancer **(Figure S6)**, suggesting that they are
301 tumor-promoting and/or essential genes that are shared by multiple pathways during lung cancer

302 growth. Thus, this counter-screen not only localized the effect of *Hras* and *Nras* inactivation but
303 also clarifies the general requirement for these genes, highlighting the value of this approach in
304 uncovering alterations that are synthetic lethal within and/or across oncogenic contexts.
305

306 **DISCUSSION**

307 Oncogenic KRAS-driven lung cancer is a leading cause of cancer-related deaths.
308 However, despite having been identified almost half a century ago, most knowledge of KRAS is
309 still limited to canonical RAS pathways such as RAF-MEK-ERK and PI3K-AKT, while the
310 functions of other RAS-interacting proteins are still largely unknown. In this study, by
311 integrating AP/MS data from human cancer cells with somatic cell CRISPR/Cas9-editing in
312 autochthonous mouse models, we assess the functional impact of inactivating a panel of KRAS-
313 interacting proteins on lung cancer *in vivo* in a multiplexed manner. Our results suggest a model
314 in which heterotypic interactions between RAS paralogs suppress oncogenic RAS-driven lung
315 cancer progression.

316 All RAS family proteins, HRAS, NRAS and KRAS (including both the KRAS4A and
317 KRAS4B splice isoforms), have been reported as dimers and nanoclusters (40-43). Importantly,
318 both *in vitro* and *in vivo* studies suggest that KRAS dimerization is required for effector protein
319 activation, cellular transformation, and tumor progression (39). Furthermore, a recent study
320 emphasized the role of oncogenic KRAS-wildtype KRAS heterodimers in lung cancer initiation,
321 progression, and therapeutic sensitivity (32). Multiple lines of evidence, including oncogenic
322 *KRAS* copy number gain, and loss of the wild-type *KRAS* allele in human tumors, as well as
323 functional studies in mouse models, suggest that wild-type KRAS is tumor-suppressive (also
324 called "RAS allelic imbalance"), although the exact role of wild-type RAS in lung cancer is still

controversial (3,33,35,45,46). Recent data have also suggested that interactions among H-, N- and KRAS proteins exist, thus raising the question of the roles of wild-type HRAS and NRAS in oncogenic KRAS-driven cancer (14,15,43).

In this study, we identified wild-type HRAS and NRAS as potent KRAS-specific tumor suppressors that directly interact with oncogenic KRAS, disrupt KRAS-KRAS interaction, and suppress RAS/MAPK signaling. Knockout of *HRAS* or *NRAS* in the context of oncogenic KRAS led to an increase in downstream MAPK signaling (**Figure 4**). Critically, this was also associated with an increase in sensitivity to treatment with a MEK inhibitor (**Figure 4**). Interestingly, our *in vitro* experiments also identified two rare, patient-derived *HRAS* mutations, $HRAS^{T50M}$ and $HRAS^{R123C}$, which are incapable of disrupting $KRAS^{G12D}$-$KRAS^{G12D}$ interaction, and would therefore offer fitness advantages to oncogenic KRAS-driven cancer. These results suggest that modulating RAS protein interactions, such as by skewing the usage of wild-type RAS and forcing inter-paralog competition, could lead to novel therapeutic strategies in the future. Moreover, analysis of mutations in non-oncogenic RAS proteins may be informative in evaluating effective treatments. However, the specific dynamics of intracellular RAS homo- and heterodimer switching, as well as the importance of these dimerization-deficient mutations in oncogenesis, may require further study.

Given the complexity of RAS signaling, other non-mutually exclusive mechanisms should be considered. For example, it has been reported that upstream regulators, such as SOS1, could bridge the interaction between oncogenic and wild-type RAS (47). Given that wild-type RAS has 5-10 times more GTPase activity than oncogenic RAS, it is possible that wild-type HRAS and NRAS could compete for upstream guanine nucleotide exchange factors with oncogenic KRAS and thus reduce RAS signaling (48). In addition, although we provide evidence

348 that inactivation of *Hras* and *Nras* have no impact on BRAF^{V618E}-driven lung cancer, it is
349 possible that they can compete with other BRAF-independent downstream effectors of
350 oncogenic KRAS. Whether HRAS and NRAS also function through these alternative routes, and
351 how different mechanisms are synchronized to execute their tumor-suppressive functions, will
352 require additional investigation.

353 In 2015, the National Cancer Institute released the "RAS Pathway V2.0", containing
354 more than 200 proteins involved in RAS signaling, and representing more than a half-century of
355 research. Building on this work, our study outlines a technological avenue to study KRAS-
356 specific signaling components in a multiplexed manner. First, by harnessing the power of
357 AP/MS and Tuba-seq, we can quantitively define tumor suppressor genes, tumor promoting
358 genes, and essential genes in RAS signaling. Second, by placing novel candidate proteins in the
359 context of a known reference “ladder” of tumor suppressors, we provide a platform in which the
360 tumor-suppressive effects of different RAS signaling components can be measured on the same
361 scale, and different studies can corroborate each other. Third, by performing a pairwise dropout
362 screen in Kras^{G12D}-driven and Braf^{V618E}-driven mouse lung cancer models, we are able to
363 identify KRAS-specific signaling components in a multiplexed manner. These novel
364 technologies will facilitate weighting different component genes in their relationship with RAS
365 and their effects in RAS-driven oncogenicity, which may be highly informative for the future
366 creation of the RAS Pathway V3.0.

367 In conclusion, via *in vivo* CRISPR/Cas9-mediated somatic genome editing, we outline a
368 technological avenue to study the function of KRAS-interacting proteins in lung cancer in a
369 multiplexed manner, and we highlight the role of RAS paralog imbalance in oncogenic KRAS-
370 driven cancers.

371 **FIGURE LEGEND:**

372

373 **Figure 1. Multiplexed identification of KRAS-interacting proteins that impact**
374 **KRASG12D-driven lung cancer growth *in vivo*.**

375 **a.** Candidate mediators of KRAS-driven lung tumor growth were identified on the basis of their
376 interactions with GTP- and GDP-locked KRAS in multiple AP/MS-based protein-protein
377 interaction screens and their expression in a mouse model of Kras-driven lung adenocarcinoma.

378 **b**. Selected KRAS-interacting proteins interact with either GTP- or GDP-locked KRAS (shown
379 as NSAF in A549 cells) and their homolog is expressed in $KRAS^{G12D}$-driven lung cancer (shown
380 as TPM).

381 **c**. Bubble plot of two AP/MS experiments with GTP- and GDP-locked mutant GTPases as baits
382 (rows), showing the enrichment of selected candidate KRAS-interacting proteins (columns).
383 Dark borders indicate FDR < 0.05.

384 **d**. Schematic of tumor initiation with a pool of barcoded Lenti-sgRNA/Cre vectors (Lenti-
385 sgKrasIP-Pool/Cre). The lentiviral pool includes four Inert sgRNAs that are either non-targeting
386 (NT) or target a functionally inert locus (Neo1-3, targeting NeoR in the $R26^{LSL\text{-}tdTomato}$ allele).
387 Each barcoded lentiviral vector contains an sgRNA, Cre, and a two-component barcode
388 composed of an sgRNA identifier (sgID) and a random barcode (BC). This design allows
389 inactivation of multiple target genes in parallel followed by quantification of the resulting tumor
390 size distributions through high-throughput sgID-BC sequencing.

391 **e**. Tumors were initiated in cohorts of *KT, KT;*$H11^{LSL\text{-}Cas9}$ and *KT;*$^{p53flox/flox}$*;*$H11^{LSL\text{-}Cas9}$ mice
392 through intratracheal delivery of Lenti-sgKrasIP-Pool/Cre. Tuba-seq was performed on each

393 tumor-bearing lung 12 weeks after initiation, followed by analyses of sgID-BC sequencing data
394 to characterize the effects of inactivating each gene.
395 **f**. Tumor sizes at indicated percentiles for each sgRNA relative to the size of sgInert-containing
396 tumors at the corresponding percentiles in *KT;H11*$^{LSL\text{-}Cas9}$ mice. Genes are ordered by 95th
397 percentile tumor size, with sgInerts on the left. sgInerts are in gray, and the line at y=1 indicates
398 no effect relative to sgInert. Error bars indicate 95% confidence intervals. Percentiles that are
399 significantly different from sgInert (two-sided FDR-adjusted $p < 0.05$) are in color. Confidence
400 intervals and P-values were calculated by bootstrap resampling.
401 **g**. Comparison of 95th percentile tumor size for each sgRNA relative to the size the 95th
402 percentile tumor size of sgInert-containing tumors in *KT;H11*$^{LSL\text{-}Cas9}$ mice versus
403 *KT;p53*$^{flox/flox}$*;H11*$^{LSL\text{-}Cas9}$ mice. Error bars indicate 95% confidence intervals calculated by
404 bootstrap resampling.
405
406 **Figure 2. HRAS and NRAS are potent suppressors of KRASG12D-driven lung cancer**
407 **growth *in vivo***
408 **a,b**. A pool of barcoded Lenti-sgRNA/Cre vectors (Lenti-sgValidation/Cre) targeting candidate
409 mediators of KRAS-driven lung tumor growth identified in the initial KRAS-interacting protein
410 Tuba-seq screen was used to initiate tumors in validation cohorts of *KT and KT;H11*$^{LSL\text{-}Cas9}$ mice.
411 This lentiviral pool includes four Inert sgRNAs, as well as sgRNAs targeting *Lkb1, Rb1*, and
412 *Rbm10* as tumor suppressor controls. Each candidate gene from the initial screen is targeted with
413 three sgRNAs. Tumors were initiated through intratracheal delivery of Lenti-sgValidation/Cre,
414 and Tuba-seq was performed on each tumor-bearing lung 12 weeks after initiation, followed by
415 analyses of sgID-BC sequencing data to characterize the effects of inactivating each gene (b).

416 **c**. Fluorescence images of representative lung lobes 12 weeks after tumor initiation. Scale bars =
417 5 mm. Lung lobes are outlined with a white dashed line.
418 **d**. Tumor sizes at indicated percentiles for each sgRNA relative to the size of sgInert-containing
419 tumors at the corresponding percentiles *in KT;H11*$^{LSL\text{-}Cas9}$ mice. Genes are ordered by 95th
420 percentile tumor size, with sgInerts on the left. Note that sgLkb1 is plotted on a separate scale to
421 facilitate visualization of sgRNAs with lesser magnitudes of effect. Dashed line indicates no
422 effect relative to sgInert. Error bars indicate 95% confidence intervals. 95% confidence intervals
423 and P-values were calculated by bootstrap resampling. Percentiles that are significantly different
424 from sgInert (2-sided FDR-adjusted $p < 0.05$) are in color.
425 **e**. Targeting Hras and Nras significantly increases mean tumor size relative to sgInerts, assuming
426 a log-normal distribution of tumor sizes (LNmean). Error bars indicate 95% confidence intervals
427 calculated by bootstrap resampling.
428 **f**. Schematic of tumor initiation with individual Lenti-sgRNA/Cre vectors. Mouse number and
429 titer of the lentiviral vectors are indicated.
430 **g**. Representative fluorescence images of lungs from *KT;H11*$^{LSL\text{-}Cas9}$ mice after tumor initiation
431 with Lenti-sgRNA/Cre vectors as indicated. Scale bar = 5 mm.
432 **h**. Representative H&E images of lungs from *KT;H11*$^{LSL\text{-}Cas9}$ mice after tumor initiation with
433 Lenti-sgRNA/Cre vectors as indicated. Tumor area (percentage of total lung area) from each
434 mouse is shown as Mean ± SD. *: $p<0.05$; Scale bar = 5 mm.
435 **i**. Representative BrdU staining images of lungs from *KT;H11*$^{LSL\text{-}Cas9}$ mice after tumor initiation
436 with Lenti-sgRNA/Cre vectors as indicated. Number of Brdu^{pos} cells per field is shown as Mean
437 ± SD. **: $p<0.01$; Scale bar = 100 μm.
438

439 **Figure 3. Wild-type HRAS or NRAS constrain the growth of human KRAS-driven cancer**
440 **cell lines.**
441 **a**. Inactivation of wild type HRAS or NRAS increases growth of KRAS-mutant H23 (G12C) and
442 H727 (G12V) cells. Wild-type (sgSAFE) or HRAS- or NRAS-knockout cells were seeded in 96
443 well plates and cultured under limited serum (1%). Cell numbers were measured via CCK8 assay.
444 Points are Mean±SD of 12 wells normalized to Day 0. **: $p<0.01$
445 **b**. Re-expression of wild type HRAS suppresses proliferation of HRAS-null H23 and H727 cells.
446 TRE-HRAS cells were seeded in 96 well plates and cultured under limited serum (1%) with or
447 without 50 ng/ml Doxycycline (Dox) and cell numbers were measured via CCK8 assay. Points
448 are Mean±SD of 12 wells normalized to Day 0. **: $p<0.01$
449 **c-d**. Inactivation of HRAS or NRAS increases H23 colony formation. Wild-type (sgSAFE),
450 HRAS-knockout (sgHRAS), or NRAS-knockout (sgNRAS) H23 cells were seeded at 1000
451 cells/well in 6-well plates and grown for two weeks. Cells were stained with crystal violet. **c**.
452 Representative images. Scale bar = 5mm. **d**. Mean±SD of colony number of 12 fields. **:
453 $p<0.01$
454 **e-f**. Re-expression of wild type HRAS suppresses HRAS-null H23 cell colony formation. TRE-
455 Ctrl or TRE-HRAS H23 cells were seeded at 1000 cells/well in 6-well plates and grown with or
456 without 50 ng/ml Doxycycline (Dox) for two weeks. Cells were stained with crystal violet. **e**.
457 Representative images. Scale bar = 5mm. f. Mean±SD of colony number of 12 fields. **:
458 $p<0.01$
459 **g-k**. Inactivation of wild type HRAS or NRAS increases H23 cell growth after transplantation. **g**.
460 Schematic of tumor initiation with subcutaneous (SubQ) or intravenous (IV) transplantation of
461 H23 cells with inactivation of HRAS or NRAS in NSG mice. Mouse number, cell number, and

462 tumor growth time after transplantation are indicated. **h**. Tumor weight from SubQ
463 transplantation of indicated cells. Each dot represents a mouse. Mean value was shown. **i**. Ki67^{pos}
464 cell number in tumor section from SubQ transplantation of indicated cells was shown as
465 Mean±SD value of 20 view fields. **j**. Tumor area (percentage of h-mitochondria^{pos} area) from IV
466 transplantation of indicated cells. Each dot represents a tumor. Mean value was shown. **k**.
467 Ki67^{pos} cell number in tumor section from IV transplantation of indicated cells is shown as
468 Mean±SD value of 20 view fields (200x). *: $p<0.05$; **: $p<0.01$; ns: not significant.
469
470 **Figure 4. Wild-type RAS paralogs finetune RAS signaling**
471 **a**. Representative image of pERK staining in *KTC* mice with tumors initiated with Lenti-
472 sgRNA/Cre vectors as indicated. Quantification of pERK^{pos} cells per tumor was shown as
473 Mean±SD of 20 tumors. *: $p<0.05$; **: $p<0.01$; Scale bar: 100 μm
474 **b**. Representative image of pERK staining in subcutaneous tumor transplanted with H23 cells as
475 indicated. Quantification of pERK^{pos} cells per field was shown as Mean±SD of 20 fields. **:
476 $p<0.01$; Scale bar: 100 μm
477 **c**. Western blot analysis of sorted cancer cells from *KTC* mice transduced with Lenti-sgRNA
478 vectors as indicated. Each mouse was transduced with 300k Lenti-sgRNA for 15 weeks. Multiple
479 tumors from same mice (ear tag as indicated) were pooled for sorting and protein extraction.
480 **d**. Western blot analysis of cultured HC494 (*KPTC*) cells transduced with Lenti-sgRNA vectors
481 as indicated. HC494 cells were transduced with lentiviral vector expressing indicated sgRNA
482 and selected with puromycin to generate stable knockout cell lines. Wild-type cell (sgNeo) or
483 HRAS- or NRAS-knockout cells (sgHras, sgNras) were cultured under limited serum (1%) for 2
484 days before protein extraction.

485 **e**. Western blot analysis of cultured H23 (left) and HOP62 (right) cells transduced with Lenti-
486 sgRNA vectors as indicated. All human cells were transduced with lentiviral vector expressing
487 indicated sgRNA and selected with puromycin to generate stable knockout cell lines. Wild-type
488 cell (sgSAFE) or HRAS- or NRAS-knockout cells (sgHRAS, sgNRAS) were cultured under
489 limited serum (1%) for 2 days before protein extraction.
490 **f**. Comparison of GI50 values to MEK inhibitors trametinib among wild-type and HRAS-null
491 H23 cells under treatment of indicated dose of trametinib for four days. Cell number were
492 measured via CCK8 assay and normalized to cells treated with vehicle. Each data point was
493 shown as Mean±SD of 12 wells.
494 **g**. Western blot analysis of cultured HRAS-null H23 cells (H23-sgHRAS) re-expression HRAS
495 (TRE-HRAS) under Doxycycline (Dox) treatment. HRAS-null H23 cells were generated from
496 previous experiment as described in Figure 3a. HRAS-null H23 cells were re-transduced with
497 lentiviral vector expressing TRE-HRAS at high MOI (>5) to generate stable HRAS re-expression
498 cells (H23-sgHRAS-TRE-HRAS). To re-express HRAS, cells were treated with low dose (0, 1,
499 and 2ng/ml) Dox and cultured under limited serum (1%) for 2 days before protein extraction.
500 **h**. Comparison of GI50 values to MEK inhibitors trametinib among HRAS-null H23 cells (H23-
501 sgHRAS) re-expressing HRAS in presence (HRAS+Dox) or absence (HRAS) of Doxycycline
502 plus indicated dose of trametinib for four days. Cell number were measured via CCK8 assay and
503 normalized to cells treated with vehicle. Each data point was shown as Mean±SD of 12 wells.
504
505 **Figure 5. Wild-type RAS paralogs finetune RAS signaling through direct interaction with**
506 **oncogenic KRAS.**

507 **a**. HRAS and NRAS are shared KRAS-interacting proteins in two protein-protein interaction
508 datasets (Kelly, Kostyrko, Han et al. 2020; Broyde, Simpson, Murray et al. 2020). Shared
509 KRAS-interaction proteins are shown as their $\log_{10}$NSAF and SigMap Score.
510 **b**. All three RAS proteins are able to disrupt $KRAS^{G12D}$-$KRAS^{G12D}$ interaction. U2OS-764 (nl-
511 $KRAS^{G12D}$/cl-$KRAS^{G12D}$) or U2OS-794 (nl-CVIM/cl-CVIM) cells expressing KRAS, HRAS, or
512 NRAS were cultured in limited serum (1%) under 100 ng/ml Doxycycline (Dox) for 24 hours.
513 ReBiL2.0 assay was performed as previously described and detailed in Methods. Points are
514 Mean±SD ReBiL2.0 score of 36 wells normalized to cells transduced with empty lentiviral
515 vector. **: $p<0.01$,
516 **c**. $HRAS^{T50M}$ and $HRAS^{R123C}$ are novel dimerization deficient mutations. U2OS-764 (nl-
517 $KRAS^{G12D}$/cl-$KRAS^{G12D}$) cells expressing wild-type or rare mutant HRAS were cultured in
518 limited serum (1%) under 100 ng/ml Dox for 24 hours. Points are Mean±SD ReBiL2.0 score of
519 12 wells normalized to cells transduced with empty lentiviral vector. **: $p<0.01$; ns: not
520 significant.
521 **d**. Cluster map of RAS effector prey proteins enriched in each experiment with the indicated
522 baits in A549 cells (for K-, H-, or N-RAS) or HEK293 cells (for KRAS). Both GTP- and GDP-
523 bond HRAS behave like GDP-bond KRAS in their RAS effector interactions.
524 **e**. Western blot analysis of cultured HRAS-null HOP62 cells (HOP62-Cas9-sgHRAS) re-
525 expressing wild-type or dimerization deficient mutations (T50M, Y64A, or R123C) under Dox
526 treatment. Cells were cultured under limited serum (1%) for 2 days before protein extraction. Re-
527 expression of dimerization deficient mutations have no effects on ERK phosphorylation.
528 **f**. Cell proliferation of cultured HRAS-null HOP62 cells (HOP62-Cas9-sgHRAS) re-expressing
529 wild-type or dimerization deficient mutations (T50M, Y64A, or R123C) under Dox treatment.

530 Cells were cultured in limited serum (1%) with or without Dox for 4 days. Cell viability was
531 measured via CCK8 assay and normalized to cells treated with vehicle. Re-expression of
532 dimerization deficient mutations have no effects on cell proliferation.
533
534 **Figure 6. Paired screen in KRAS-driven and BRAF-driven lung cancer models validates**
535 **Hras and Nras as Kras-specific tumor suppressors.**
536 **a-b**. Schematic of pairwise screen of tumor suppressive function in Kras- and Braf-driven lung
537 cancer. A pool of barcoded Lenti-sgRNA/Cre vectors targeting top mediators of Kras-driven
538 lung tumor growth (Lenti-sgMultiGEMM/Cre) was used to initiate tumors in cohorts of
539 *KT;H11*$^{LSL\text{-}Cas9}$ and *Braf*$^{LSL\text{-}V600E/+}$*T;H11*$^{LSL\text{-}Cas9}$ (*BrafT;H11*$^{LSL\text{-}Cas9}$) mice. Each mediator of
540 KRAS-driven tumor growth (*Hras, Nras, Nme2* and *Fnta*) was targeted by two sgRNAs (those
541 with the largest effect size in the validation screen). The pool also included four Inert sgRNAs,
542 as well as sgRNAs targeting *Apc, Cdkn2a,* and *Rbm10* as tumor suppressor controls (**a**). Tumors
543 were initiated through intratracheal delivery of Lenti-sgMultiGEMM/Cre, and Tuba-seq was
544 performed on each tumor-bearing lung 15 weeks after initiation, followed by analysis of sgID-
545 BC sequencing data to characterize the effects of inactivating each gene (**b**).
546 **c**. Fluorescence images of representative lung lobes 15 weeks after tumor initiation. Scale bars =
547 5 mm. Lung lobes are outlined with a white dashed line.
548 **d**. Total lung weight in *KT; H11*$^{LSL\text{-}Cas9}$ and *BrafT;H11*$^{LSL\text{-}Cas9}$ mice 15 weeks after tumor
549 initiation. Each dot is a mouse and mean value is indicated. **: $p<0.01$
550 **e-f**. Size distribution of sgInert tumors in *KT; H11*$^{LSL\text{-}Cas9}$ and *BrafT;H11*$^{LSL\text{-}Cas9}$ mice. In **e**., each
551 dot represents a tumor, and the area of each dot is proportional to the number of cancer cells in
552 that tumor. To prevent overplotting a random sample of 1,000 tumors from each of five

553 representative *KT; H11*$^{LSL\text{-}Cas9}$ and *BrafT;H11*$^{LSL\text{-}Cas9}$ mice are plotted. In **f**., the empirical
554 cumulative distribution function of tumor sizes across all *KT; H11*$^{LSL\text{-}Cas9}$ and *BrafT;H11*$^{LSL\text{-}Cas9}$
555 mice is plotted. Tumors >500 cells in size are shown.
556 **g**. Inactivation of Hras and Nras increases tumor size in *KT; H11*$^{LSL\text{-}Cas9}$ but not *BrafT;H11*$^{LSL\text{-}Cas9}$
557 models. Tumor sizes at indicated percentiles for each sgRNA relative to the size of sgInert-
558 containing tumors at the corresponding percentiles in *KT; H11*$^{LSL\text{-}Cas9}$ (left, white background)
559 and *BrafT;H11*$^{LSL\text{-}Cas9}$ (right, gray background) mice. Line at y=1 indicates no effect relative to
560 sgInert. Error bars indicate 95% confidence intervals. Percentiles that are significantly different
561 from sgInert (two-sided FDR-adjusted $p < 0.05$) are in color. Confidence intervals and P-values
562 were calculated by bootstrap resampling.
563 **h**. Comparison of the effects of inactivation of known tumor suppressors (*Rbm10, Apc*, and
564 *Cdkn2a*) on tumor size in *BrafT;H11*$^{LSL\text{-}Cas9}$ models. Tumor sizes at indicated percentiles for each
565 sgRNA relative to the size of sgInert-containing tumors at the corresponding percentiles in *KT;*
566 *H11*$^{LSL\text{-}Cas9}$ (left, white background) and *BrafT;H11*$^{LSL\text{-}Cas9}$ (right, gray background) mice. Line at
567 y=1 indicates no effect relative to sgInert. Error bars indicate 95% confidence intervals.
568 Percentiles that are significantly different from sgInert (two-sided FDR-adjusted $p < 0.05$) are in
569 color. Confidence intervals and P-values were calculated by bootstrap resampling.
570 **i**. Schematic of wild-type RAS paralogs function as tumor suppressors in oncogenic KRAS
571 signaling. Left panel, in oncogenic KRAS-driven lung cancer cells, wild-type RAS paralogs
572 competitively interact with oncogenic KRAS and suppress oncogenic KRAS-KRAS interaction.
573 Right panel, inactivation of wild-type RAS allele, or "RAS paralog imbalance", hyper-activated
574 oncogenic KRAS signaling and promotes lung cancer growth.
575

576 **Supplemental Figure 1. Tumor barcoding coupled with barcode sequencing (Tuba-seq) can**
577 **uncover engineered alterations that reduce tumor number and growth.**
578 **a-b**. Schematic of the Tuba-seq approach to measure the effects of essential gene inactivation on
579 tumor growth. Lentiviral-sgRNA/Cre vectors with inert sgRNAs (gray) or sgRNAs targeting
580 known essential genes (navy) were diversified with a two component sgID-BC. A vector
581 targeting known tumor suppressor Apc was included as a positive control (**a**). Tumors were
582 initiated with this barcoded Lenti-sgEssential/Cre pool in *KT and KT;H11*$^{LSL\text{-}Cas9}$ mice. Tuba-seq
583 was performed on each tumor-bearing lung 12 weeks after initiation, followed by analyses of
584 sgID-BC sequencing data to characterize the effects of inactivating each gene (**b**).
585 **c**. Tumor sizes at indicated percentiles for each sgRNA relative to the size of sgInert-containing
586 tumors at the corresponding percentiles. Line at y=1 indicates no effect relative to sgInert. Error
587 bars indicate 95% confidence intervals. Percentiles that are significantly different from sgInert
588 (two-sided FDR-corrected $p < 0.05$) are in color. Confidence intervals and P-values were
589 calculated by bootstrap resampling.
590 **d**. The impact of each sgRNA on mean tumor size relative to sgInerts, assuming a log-normal
591 distribution of tumor sizes (LNmean). sgRNAs with two-sided $P<0.05$ after FDR-adjustment are
592 in bold.
593 **e**. The impact of each sgRNA on tumor burden (number of neoplastic cells aggregated across all
594 tumors of a genotype) relative to sgInerts and normalized to the same statistic in *KT* mice to
595 account for representation of each sgRNA in the viral pool. sgInerts are in gray and the line at
596 y=1 indicates no effect. Error bars indicate 95% confidence intervals. Relative burdens
597 significantly different from sgInert (two-sided FDR-corrected $p<0.05$) are in color. Confidence
598 intervals and P-values were calculated by bootstrap resampling.

599 **f**. The impact of each sgRNA on tumor number relative to sgInerts and normalized to the same
600 statistic in *KT* mice to account for representation of each sgRNA in the viral pool. sgInerts are in
601 gray and the line at y=1 indicates no effect. Error bars indicate 95% confidence intervals.
602 Relative tumor numbers significantly different from sgInert (two-sided FDR-corrected $p<0.05$)
603 are in color. Confidence intervals and P-values were calculated by bootstrap resampling.
604 **g**. The impact of each sgRNA on tumor number plotted against its impact on LNmean tumor size.
605 The lines at y=1 and x=1 indicate no effect relative to sgInert on tumor number and size,
606 respectively. sgRsp19 and sgPcna cluster in the lower left quadrant near x=1, indicating that
607 targeting essential genes strongly reduces tumor number but only moderately decreases average
608 tumor size. Error bars indicate 95% confidence intervals calculated by bootstrap resampling.
609
610 **Supplemental Figure 2. Inactivation of KRAS-interacting proteins has similar impacts on**
611 **tumor growth in p53-proficient and p53-deficient contexts.**
612 **a**. Tumor sizes at indicated percentiles for each sgRNA relative to the size of sgInert-containing
613 tumors at the corresponding percentiles in *KT* mice. *KT* mice lack Cas9, thus all sgRNAs are
614 functionally equivalent to sgInerts. Genes are ordered as in Figure **1f**. Line at y=1 indicates no
615 effect relative to sgInert. Error bars indicate 95% confidence intervals. Confidence intervals and
616 P-values were calculated by bootstrap resampling. As expected, no percentiles were significantly
617 different from sgInert (two-sided FDR-adjusted $p < 0.05$).
618 **b**. The impact of each sgRNA on mean tumor size relative to sgInerts in $KT;H11^{LSL\text{-}Cas9}$,
619 assuming a log-normal distribution of tumor sizes (LNmean). sgRNAs with two-sided $P<0.05$
620 after FDR-adjustment are in bold. P-values were calculated by bootstrap resampling.

621 **c-d**. The impact of each sgRNA on tumor burden (c) and number (d) relative to sgInerts in
622 *KT;H11*$^{LSL\text{-}Cas9}$ mice, normalized to the corresponding statistic in *KT* mice to account for
623 representation of each sgRNA in the viral pool. sgInerts are in gray and the line at y=1 indicates
624 no effect. Error bars indicate 95% confidence intervals. Relative tumor burdens and numbers
625 significantly different from sgInert (two-sided FDR-adjusted p<0.05) are in color. Confidence
626 intervals and P-values were calculated by bootstrap resampling.
627 **e**. Tumor sizes at the indicated percentiles for each sgRNA relative to the size of sgInert-
628 containing tumors in *KT;p53*$^{flox/flox}$*;H11*$^{LSL\text{-}Cas9}$ mice. Genes are ordered as in Figure **1f**. Dashed
629 line indicates no effect relative to sgInert. Error bars indicate 95% confidence intervals.
630 Percentiles that are significantly different from sgInert (two-sided FDR-adjusted p < 0.05) are in
631 color. Confidence intervals and P-values calculated by bootstrap resampling.
632 **f-h**. Comparison of the impact of each sgRNA on relative LNmean tumor size (**f**), tumor burden
633 (**g**) and tumor number (**h**) in *KT;H11*$^{LSL\text{-}Cas9}$ and *KT;p53*$^{flox/flox}$*;H11*$^{LSL\text{-}Cas9}$ mice. Error bars
634 indicate 95% confidence intervals calculated by bootstrap resampling.
635
636 **Supplemental Figure 3. Top candidate KRAS-interacting proteins from initial Tuba-seq**
637 **screen impact multiple metrics of tumor growth in validation cohort.**
638 **a.** Tumor sizes at indicated percentiles for each sgRNA relative to the size of sgInert-containing
639 tumors at the corresponding percentiles in *KT* mice. *KT* mice lack Cas9, thus all sgRNAs are
640 functionally equivalent to sgInerts. Genes are ordered as in Figure **2d** but note the change in axis
641 scaling. Line at y=1 indicates no effect relative to sgInerts. Error bars indicate 95% confidence
642 intervals. Confidence intervals and P-values were calculated by bootstrap resampling. As
643 expected, no percentiles were significantly different from sgInert (FDR-adjusted p < 0.05).

644 **b.** The impact of each sgRNA on mean tumor size relative to sgInerts, assuming a log-normal
645 distribution of tumor sizes (LNmean). Two-sided P-values were calculated by bootstrap
646 resampling. sgRNAs with P<0.05 after FDR-adjustment are in bold. Note that this data for the
647 sgInerts, sgHras#1-3 and sgNras#1-3 is also plotted in Figure 2e.
648 **c.** The impact of each sgRNA on tumor burden relative to sgInerts in *KT;H11*$^{LSL\text{-}Cas9}$ mice,
649 normalized to the corresponding statistic in *KT* mice to account for representation of each
650 sgRNA in the viral pool. sgInerts are in gray and the line at y=1 indicates no effect. Error bars
651 indicate 95% confidence intervals. Relative tumor burdens significantly different from sgInert
652 (two-sided FDR-adjusted p<0.05) are in color. Confidence intervals and P-values were
653 calculated by bootstrap resampling.
654 **d**. The impact of each sgRNA on tumor number relative to sgInerts in *KT;H11*$^{LSL\text{-}Cas9}$ mice,
655 normalized to the corresponding statistic in *KT* mice to account for representation of each
656 sgRNA in the viral pool. sgInerts are in gray and the line at y=1 indicates no effect. Error bars
657 indicate 95% confidence intervals. Relative tumor numbers significantly different from sgInert
658 (two-sided FDR-adjusted p<0.05) are in color. Confidence intervals and P-values were
659 calculated by bootstrap resampling.
660
661 **Supplemental Figure 4. Dependency of RAS family member across human LUAD cell lines.**
662 **a.** Distribution of dependency scores for each RAS family member across human LUAD cell
663 lines divided by KRAS mutation status. **** (p <0.0001), ns (not significant).
664 **b.** Volcano plot showing effects of RAS gene knockouts in A549 cells. (Data source: Marcus
665 Robert Kelly, Kaja Kostyrko, Kyuho Han, et al. 2020)

666 **c.** Volcano plot showing effects of RAS gene knockouts in KRAS-mutant human LUAD cells
667 (left: H2009, mid: H23, right: H1975) in 3D culture. (Data source: Kyuho Han, et al. 2020)
668
669 **Supplemental Figure 5. Inactivation of wild type HRAS or NRAS increases H23 cell growth**
670 **after transplantation.**
671 **a.** Representative image of subcutaneous tumor size four weeks after transplantation with H23
672 cells as indicated. Quantification was shown in Figure **3h**. Scale bar: 2 mm
673 **b.** Representative image of Ki67 staining from subcutaneous tumor four weeks after
674 transplantation with H23 cells as indicated. Quantification was shown in Figure **3i**. Scale bar:
675 100 μm
676 **c.** Representative image of HE (upper) and human mitochondria (lower) staining from lung
677 tumor four weeks after intravenous transplantation with H23 cells as indicated. Quantification
678 was shown in Figure **3j**. Scale bar: 200 μm
679 **d.** Representative image of Ki67 staining from lung tumor four weeks after intravenous
680 transplantation with H23 cells as indicated. Quantification was shown in Figure **3k**. Scale bar:
681 200 μm
682
683 **Supplemental Figure 6. Additional data from paired screen of Kras-interacting modulators**
684 **of tumor growth in Kras-driven and Braf-driven lung cancer models**
685 **a-c**. Tumor sizes at indicated percentiles for each sgRNA relative to the size of sgInert-
686 containing tumors at the corresponding percentiles in *KTC* (a), *BrafTC* (b) and *KT* mice (c).
687 Genes are ordered by 95th percentile tumor size in *KTC* mice, with sgInerts on the left. sgInerts
688 are in gray, and line at y=1 indicates no effect relative to sgInert. Error bars indicate 95%

689 confidence intervals. Percentiles that are significantly different from sgInert (two-sided FDR-
690 adjusted $p < 0.05$) are in color. Confidence intervals and P-values were calculated by bootstrap
691 resampling.
692 **d**. The impact of each sgRNA on tumor burden relative to sgInerts in *KTC* (top) and *BrafTC*
693 (bottom) mice, normalized to the corresponding statistic in *KT* mice to account for representation
694 of each sgRNA in the viral pool. sgInerts are in gray and the line at y=1 indicates no effect. Error
695 bars indicate 95% confidence intervals. Relative tumor burdens significantly different from
696 sgInert (two-sided FDR-adjusted $p<0.05$) are in color. Confidence intervals and P-values were
697 calculated by bootstrap resampling.
698 **d.** The impact of each sgRNA on tumor number relative to sgInerts in *KTC* (top) and *BrafTC*
699 (bottom) mice, normalized to the corresponding statistic in *KT* mice to account for representation
700 of each sgRNA in the viral pool. sgInerts are in gray and the line at y=1 indicates no effect. Error
701 bars indicate 95% confidence intervals. Relative tumor numbers significantly different from
702 sgInert (two-sided FDR-adjusted $p<0.05$) are in color. Confidence intervals and P-values were
703 calculated by bootstrap resampling.
704
705
706
707
708
709
710
711

712

713

714

715 **METHODS**

716 *Cells, Reagents and Plasmids:*

717 H23, H727, and HOP62 cells were originally purchased from ATCC; HC494(*KPT*) lung
718 adenocarcinoma cells were generated in the Winslow Lab; U2OS-134-764np (nl-KRAS^{G12D} cl-
719 KRAS^{G12D}; KRAS^{G12D} was fused to the N-termini of split luciferase proteins) and U2OS-134-
720 794p (nl-CVIM cl-CVIM; CVIM represents the C-terminal last 20 amino acids of KRAS4B)
721 cells were generated in the Wahl lab by Dr. Yao-Cheng Li (Salk Institute for Biological Studies).
722 HC494 cells were cultured in DMEM containing 10% FBS, 100 units/mL penicillin and 100
723 μg/mL streptomycin. A549, H460 and H82 cells were cultured in RPMI1640 media containing
724 10% FBS, 100 units/mL penicillin and 100 μg/mL streptomycin. U2OS cells were cultured in
725 DMEM/F12 (Thermo Fisher; phenol-red free), 10% (vol/vol) FBS, and 10 μg/mL ciprofloxacin.
726 All cell lines were confirmed to be mycoplasma negative (MycoAlert Detection Kit, Lonza).
727 Trametinib was purchased from MedChemExpress (HY-10999); 5-Bromo-2′-deoxyuridine
728 (10280879001) and D-Luciferin (L9504-5MG) was purchased from Sigma-Aldrich.

729

730 *Design, generation, barcoding, and production of lentiviral vectors*

731 The sgRNA sequences targeting the putative tumor suppressor genes were designed using
732 CRISPick (https://portals.broadinstitute.org/gppx/crispick/public). All sgRNA sequence are
733 shown in Supplementary Table 2. Each desired sgRNA vector was modified from our previously
734 published pll3-U6-sgRNA-Pgk-Cre vector via site-directed mutagenesis (New England Biolabs,

735 E0554S). The generation of the barcode fragment containing the 8-nucleotide sgID sequence and
736 20-nucleotide degenerate barcode, and subsequent ligation into the vectors were performed as
737 previously described.
738 Lentiviral vectors were produced using polyethylenimine (PEI)-based transfection of 293T cells
739 with the plasmids indicated in Supplementary Table 1, along with delta8.2 and VSV-G
740 packaging plasmids in 150-mm cell culture plates. Sodium butyrate (Sigma Aldrich, B5887) was
741 added 8 hours after transfection to achieve a final concentration of 20 mM. Medium was
742 refreshed 24 hours after transfection. 20 mL of virus-containing supernatant was collected 36,
743 48, and 60 hours after transfection. The three collections were then pooled and concentrated by
744 ultracentrifugation (25,000 rpm for 1.5 hours), resuspended overnight in 100 µL PBS, then
745 frozen at -80°C and were thawed and pooled at equal ratios immediately prior to delivery to
746 mice.
747
748 *Mice and tumor initiation*
749 The use of mice for the current study has been approved by Institutional Animal Care and
750 Use Committee at Stanford University, protocol number 26696.
751 $Kras^{LSL\text{-}G12D/+}$ (RRID:IMSR_JAX:008179), $R26^{LSL\text{-}tdTomato}$ (RRID:IMSR_JAX:007909),
752 and $H11^{LSL\text{-}Cas9}$ (RRID:IMSR_JAX:027632) mice have been previously described. They were on
753 a C57BL/6:129 mixed background. The B6.129P2(Cg)-$Braf^{tm1Mmcm}$/J ($BRAF^{F\text{-}V600E}$) mice
754 were initially generated by Dankort et al. and obtained from the Jackson Laboratory
755 (RRID:IMSR_JAX: 017837). Tumors were initiated by intratracheal delivery of 60 µl of
756 lentiviral vectors dissolved in PBS.

757 For the initial experiments in Figure 1 and 2, tumors were allowed to develop for 12 weeks after
758 viral delivery of a lentiviral pool that contained 19 barcoded Lenti-sgRNA/Cre vectors (Lenti-
759 sgKrasIP/Cre). Tumors were initiated in Kras$^{LSL\text{-}G12D}$; R26$^{LSL\text{-}tdTomato}$ (*KT*), *KT;*H11$^{LSL\text{-}Cas9}$; or
760 *KT;p53$^{fl/fl}$;*H11$^{LSL\text{-}Cas9}$ mice with 1.95x10^5 infectious units (ifu)/mouse.
761 For the validation experiments in Figure 3, tumors were allowed to develop for 15 weeks after
762 viral delivery of a lentiviral pool that contained 26 barcoded Lenti-sgRNA/Cre vectors (Lenti-
763 sgValidation/Cre). Tumors were initiated in Kras$^{LSL\text{-}G12D}$; R26$^{LSL\text{-}tdTomato}$ (*KT*) or *KT;*H11$^{LSL\text{-}Cas9}$;
764 mice with 3x10^5 ifu/mouse.
765 For the individual sgRNA tumor initiation experiments in Figure 3, tumors were allowed to
766 develop for 12 weeks after viral delivery of individual sgRNA expressing lentiviral vector that
767 targeting Neo2, Hras, or Nras. Tumors were initiated in *KT;*H11$^{LSL\text{-}Cas9}$; mice with 1x10^5
768 ifu/mouse.
769 For the paired screen experiments in Figure 6, tumors were allowed to develop for 15 weeks
770 after viral delivery of a lentiviral pool that contained 15 barcoded Lenti-sgRNA/Cre vectors
771 (Lenti-sgMultiGEMM/Cre). Tumors were initiated in *KT;*H11$^{LSL\text{-}Cas9}$ or Braf^{V600E}; R26$^{LSL\text{-}}$
772 ^{tdTomato}; H11$^{LSL\text{-}Cas9}$ mice with 3x10^5 ifu/mouse.
773
774 *Tuba-seq library generation*
775 Genomic DNA was isolated from bulk tumor-bearing lung tissue from each mouse as previously
776 described. Briefly, benchmark control cell lines were generated from LSL-YFP MEFs
777 transduced by a barcoded Lenti-sgNT3/Cre vector (NT3: an inert sgRNA with a distinct sgID)
778 and purified by sorting YFP^{pos} cells. Three benchmark control cell lines (500,000 cells each)
779 were added to each mouse lung sample prior to lysis to enable the calculation of the absolute

780 number of neoplastic cells in each tumor from the number of sgID-BC reads. Following
781 homogenization and overnight protease K digestion, genomic DNA was extracted from the lung
782 lysates using standard phenol-chloroform and ethanol precipitation methods. Subsequently, Q5
783 High-Fidelity 2x Master Mix (New England Biolabs, M0494X) was used to amplify the sgID-
784 BC region from 32 µg of genomic DNA in a total reaction volume of 800 µl per sample. The
785 unique dual-indexed primers used were Forward: AAT GAT ACG GCG ACC ACC GAG ATC
786 TAC AC-8 nucleotides for i5 index-ACA CTC TTT CCC TAC ACG ACG CTC TTC CGA
787 TCT-6 to 9 random nucleotides for increased diversity-GCG CAC GTC TGC CGC GCT G and
788 Reverse: CAA GCA GAA GAC GGC ATA CGA GAT-6 nucleotides for i7 index- GTG ACT
789 GGA GTT CAG ACG TGT GCT CTT CCG ATC T-9 to 6 random nucleotides for increased
790 diversity-CAG GTT CTT GCG AAC CTC AT. The PCR products were purified with Agencourt
791 AMPure XP beads (Beckman Coulter, A63881) using a double size selection protocol. The
792 concentration and quality of the purified libraries were determined using Agilent High
793 Sensitivity DNA kit (Agilent Technologies, 5067-4626) on the Agilent 2100 Bioanalyzer
794 (Agilent Technologies, G2939BA). The libraries were pooled based on lung weight to ensure
795 even reading depth, cleaned up again using AMPure XP beads, and sequenced (read length
796 2x150bp) on the Illumina HiSeq 2500 or NextSeq 550 platform (Admera Health Biopharma
797 Services).
798
799 *Generation of Stable Cell Lines:*
800 Parental cells were seeded at 50% confluency in a 6-well plate the day before transduction (day
801 0). The cell culture medium was replaced with 2 mL fresh medium containing 8 µg/mL
802 hexadimethrine bromide (Sigma Aldrich, H9268-5G), 20 µL ViralPlus Transduction Enhancer

803 (Applied Biological Materials Inc., G698) and 40 μL concentrated lentivirus and cultured
804 overnight (Day 1). The medium was then replaced with complete medium and cultured for
805 another 24 hours (Day 2). Cells were transferred into a 100 mm cell culture dish with appropriate
806 amounts of antibiotic (Blasticidin doses: U2OS: 10 μg/mL; HOP62: 50 μg/mL; H727: 10
807 μg/mL; H23: 15 μg/mL; Puromycin doses: HC494: 5 μg/mL; U2OS: 1 μg/mL; HOP62: 5
808 μg/mL; H727: 5 μg/mL; H23: 5 μg/mL) and selected for 48 hours (Day 3).
809
810 *Western Blot*
811 Cells were lysed in RIPA buffer (50 mM Tris-HCl (pH 7.4), 150 mM NaCl, 1% Nonidet P-40,
812 and 0.1% SDS) and incubated at 4 °C with continuous rotation for 30 minutes, followed by
813 centrifugation at 12,000 × rcf for 10 minutes. The supernatant was collected, and the protein
814 concentration was determined by BCA assay (Thermo Fisher Scientific, 23250). Protein extracts
815 (10–50 μg) were dissolved in 10% SDS-PAGE and transferred onto PVDF membranes. The
816 membranes were blocked with 5% non-fat milk in TBS with 0.1% Tween 20 (TBST) at room
817 temperature for one hour, followed by incubation with primary antibodies diluted in TBST
818 (1:1000) at 4 °C overnight. After three 10-minutes washes with TBST, the membranes were
819 incubated with the appropriate secondary antibody conjugated to HRP diluted in TBST
820 (1:10000) at room temperature for 1 hour. After three 10-minutes washes with TBST, Protein
821 expression was quantified with enhanced chemiluminescence reagents (Fisher Scientific,
822 PI80196).
823 Antibodies used in this study: HSP90 (BD Biosciences, 610418), pAKT (Cell Signaling, 4060S),
824 pERK (Cell Signaling, 4370L), ERK (Cell Signaling, 9102S), AKT (Cell Signaling, 4691S),

825 HRAS (Thermo Fisher Scientific, 18295-1-AP), NRAS (Santa Cruz Biotechnology, sc-31), HA-
826 tag (Santa Cruz Biotechnology, sc-7392).
827
828 *Histology and immunohistochemistry (IHC)*
829 Lung lobes were fixed in 4% formalin and paraffin embedded. Hematoxylin and eosin staining
830 was performed using standard methods. IHC was performed on 4-μm sections with IHC was
831 performed using Avidin/Biotin Blocking Kit (Vector Laboratories, SP-2001), Avidin-Biotin
832 Complex kit (Vector Laboratories, PK-4001), and DAB Peroxidase Substrate Kit (Vector
833 Laboratories, SK-4100) following standard protocols.
834 The following primary antibodies were used: Ki-67 (BD Pharmingen, 550609), BrdU (BD
835 Pharmingen, 555627), human mitochondria (Abcam, ab92824), pERK (Cell Signaling, 4370L).
836 Total tumor burden (tumor area/total area × 100%), mitochondria^{pos} tumor burden
837 (mitochondria^{pos} area/total area × 100%), BrdU^{pos} cell number, Ki67^{pos} cell number, and pERK^{pos}
838 cell number were calculated using ImageJ. All ImageJ macros were uploaded.
839
840 *Cell proliferation assay (CCK8)*
841 For cell proliferation assays, cells were seeded in 96-well plates at a density of 5000 cells per
842 well and allowed to adhere overnight in regular growth media (Day 0). Cells were then cultured
843 in media as indicated on each figure panel for 7 days. Relative cell number were measured every
844 other day using Cell Counting Kit-8 (Bimake, B34304) according to the manufacturer's
845 instructions.
846
847 *Colony formation assay*

848 For clonogenic assays, cells were seeded in 6-well plates at a density of 500 cells per well
849 and allowed to adhere overnight in regular growth media. Cells were then cultured in media as
850 indicated on each figure panel for 14 days. Growth media with or without drugs was replaced
851 every 2 days. At the end point, cells were stained with 0.5% crystal violet in 20% methanol.
852 Colony numbers were calculated using ImageJ. All ImageJ macros were uploaded.
853
854 *Allograft studies in immunocompromised mice*
855 For intravenous transplants into immunocompromised NSG mice, $5x10^5$ H23 cells were injected
856 into one of lateral tail veins. Mice were sacrificed 28 days post-injection and lung lobe were
857 fixed in 4% formalin and paraffin embedded. For subcutaneous transplants into
858 immunocompromised NSG mice, 2×10^6 of each H23 cells (sgSAFE, sgHRAS, and sgNRAS)
859 were re-suspended in 200uL Matrigel® Basement Membrane Matrix (Corning, 354234) and
860 injected into three parallel sites per mouse. Mice were sacrificed 28 days post-injection. Tumors
861 were dissected and the weight, height, width, and length, of each tumor was measured. Tumor
862 volume was roughly calculated via the formula: $V = (4/3) \times \pi \times (L/2) \times (L/2) \times (D/2)$.
863 Institute of Medicine Animal Care and Use Committee approved all animal studies and
864 procedures.
865
866 *ReBiL2.0 assay*
867 ReBiL2.0 assay was performed as previously descried. ReBiL cells (U2OS-134-764np or U2OS-
868 134-794p with overexpression of KRAS4b, HRAS or NRAS) were seeded in i) 96-well plates at
869 density of $2x10^4$, and ii) 6-well plates at density of $1x10^6$ and allowed to adhere overnight in
870 regular growth media (DMEM/F12, 10% FBS, and 10 μg/mL ciprofloxacin). The next day, cells

871 were then cultured in serum limited media (DMEM/F12, 1% FBS, and 10 μg/mL ciprofloxacin)
872 containing 100 ng/mL doxycycline for 24 hours. Upon termination of the ReBiL assay, i) to
873 measure raw luciferase activity, 300 μM D-luciferin was added to 96-well plate culture and
874 incubate in 37ºC for 30mins and raw luminescent data collected by a Tecan microplate reader; ii)
875 to measure viable cell numbers, CCK-8 assay were performed in the same 96-well plate culture
876 and raw cell number data collected by a Tecan microplate reader; iii) to quantify the 1/2luc
877 fusion proteins, ReBiL cells from 6-well plate culture were harvested with RIPA lysis buffer for
878 protein extraction and western blot was performed for HA-tag and HSP90 expression. Then the
879 ReBiL2.0 score was calculated via the formula:
880 ReBiL2.0 score = ([Raw Luminescence]/[Cell number]) / ([1/2luc Least]/[HSP90])
881
882 *Analysis of human lung adenocarcinoma cancer genome sequencing data (for HRAS rare*
883 *mutations)*
884 To assess evidence that *HRAS* functions as a Kras-specific tumor suppressor in human
885 cancer, we queried publicly available cancer genomic datasets. GENIE Release 9.1-public was
886 accessed through the Synapse platform and data on somatic mutations
887 (data_mutations_extended.txt), sample- and patient-level clinical data (data_clinical_sample.txt
888 and data_clinical_patient.txt), and genotyping panel information (genomic_information.txt) were
889 downloaded. TCGA data were accessed through the GDC hub of the UCSC Xena Browser.
890 MuTect2 somatic mutation calls for all cancer types and sample- and patient-level clinical data
891 (GDC-PANCAN.basic_phenotype.tsv) were downloaded. Both datasets were filtered to only
892 include lung adenocarcinoma samples, and each sample was assigned to its patient of origin.
893 There were 597 lung adenocarcinoma samples with genotype information in TCGA and

894 Samples were then annotated for the presence of an oncogenic Kras mutation (a missense
895 mutation in Kras exons 12, 13 or 61) and for the presence of potentially functional Hras
896 mutations (variants that were silent, intergenic, intronic, or fell in the 3' or 5' UTRs were
897 excluded from this analysis). From this information we produced a list of the frequency of all
898 Hras variants in lung adenocarcinoma samples with and without oncogenic Kras in both datasets.
899 The genotyping panel information was used to identify GENIE samples that were not genotyped
900 at Hras and exclude these from the frequency calculation.

901 While it is unclear how our findings may extrapolate to other cancer types, Hras
902 mutations are exceedingly rare (occurring at a frequency of ~0.008 in GENIE samples and
903 ~0.005 in TCGA samples) so we therefore also performed a pair of pan-cancer analyses where
904 the steps described above were performed without first filtering to include only lung
905 adenocarcinoma.

906

907 *Process paired-end reads to identify the sgID and barcode*

908 Sequencing of Tuba-seq libraries produces reads that are expected to contain an 8-
909 nucleotide sgID followed by a 30-nucleotide barcode (BC) of the form
910 GCNNNNNTANNNNNGCNNNNNTANNNNNGC, where each of the 20 Ns represent random
911 nucleotides. Each sgID has a one-to-one correspondence with an sgRNA in the viral pool; thus,
912 the sgID sequence identifies the gene targeted in a given tumor. Note that all sgID sequences in
913 the viral pool differ from each other by at least three nucleotides such that incorrect sgID
914 assignment (and thus, inference of tumor genotype) due to PCR or sequencing error is extremely
915 unlikely. The random 20-nucleotide portion of the BC is expected to be unique to each lentiviral
916 integration event, and thus tags all cells in a single clonal expansion. Note that the length of the

917 barcode ensures a high theoretical potential diversity (~$4^{20} > 10^{12}$ barcodes per vector), so while
918 the actual diversity of each Lenti-sgRNA/Cre vector is dictated by the number of colonies
919 generated during the plasmid barcoding step, it is very unlikely that we will observe the same BC
920 in multiple clonal expansions.

921 FASTQ files were parsed using regular expressions to identify the sgID and BC for each
922 read. To minimize the effects of sequencing error on BC identification, we required the forward
923 and reverse reads to agree completely within the 30-nucleotide sequence to be further processed.
924 We also screened for barcodes that were likely to have arisen due to errors in sequencing the
925 barcodes of genuine tumors. Given the low rate of sequencing error, we expect these spurious
926 "tumors" to have read counts that are far lower than the read counts of the genuine tumors from
927 which they arise. While it is impossible to eliminate these spurious tumors, we sought to
928 minimize their effect by identifying small "tumors" with barcodes that are highly similar to the
929 barcodes of larger tumors. Specifically, if a pair of "tumors" had barcodes that were within a
930 Hamming distance of two, and if one of the tumors had less than 5% as many reads as the other,
931 then the reads associated with the smaller tumor were attributed to the larger tumor.

932 After these filtering steps, the read counts associated with each barcode were converted to
933 absolute neoplastic cell numbers by normalizing to the number of reads in the "spike-in" cell
934 lines added to each sample prior to lung lysis and DNA extraction. The median sequencing depth
935 across experiments was ~1 read per 6.4 cells.

936 For statistical comparisons of tumor genotypes, we applied a minimum tumor size cutoff
937 of 100 cells. In selecting a cutoff, we sought to include tumors that are large enough to be
938 consistently detected despite differences in sequencing depth among mice, while using as many
939 tumors as possible to maximize the statistical power. Importantly, we analyzed each Tuba-seq

940 dataset with multiple minimum tumor size cut-offs (50, 100, 200, 500 cells) and found that our
941 findings were robust.
942
943 *Summary statistics for overall growth rate*
944 To assess the extent to which a given gene (*X)* affects tumor growth, we compared the
945 distribution of tumor sizes produced by vectors targeting that gene (sg*X* tumors) to the
946 distribution produced by our negative control vectors (sg*Inert* tumors). We relied on two
947 statistics to characterize these distributions: the size of tumors at defined percentiles of the
948 distribution (specifically the 50th, 60th, 70th, 80th, 90th, and 95th percentile tumor sizes), and the
949 log-normal mean size (LN mean). The percentile sizes are nonparametric summary statistics of
950 the tumor size distribution. In considering percentiles corresponding to the right tail of the
951 distribution, we focus on the growth of larger tumors, thereby avoiding issues stemming from
952 potential variation in cutting efficiency among guides. The LN mean is the maximum-likelihood
953 estimate of mean tumor size assuming a log-normal distribution. Previous work found that this
954 statistic represents the best parametric summary of tumor growth based on the maximum
955 likelihood quality of fit of various common parametric distributions.
956
957 To quantify the extent to which each gene suppressed or promoted tumor growth, we
958 normalized statistics calculated on tumors of each genotype to the corresponding inert statistic.
959 The resulting ratios reflect the growth advantage (or disadvantage) associated with each tumor
960 genotype relative to the growth of *sgInert* tumors.
961
962 For example, the relative i^{th} percentile size for tumors of genotype X was calculated as:

963

964 $$Relative\ size\ at\ i^{th}\ percentile_{sgX} = \frac{i^{th}\ percentile\ of\ sgX\ distribution}{i^{th}\ percentile\ of\ sgInert\ distribution}$$

965

966 Likewise, the relative LN mean size for tumors of genotype X was calculated as:

967

968 $$Relative\ LNmean_{sgX} = \frac{LNmean\ of\ sgX\ distribution}{LNmean\ of\ sgInert\ distribution}$$

969

970 *Summary statistics for relative tumor number and relative tumor burden*

971 In addition to the tumor size metrics described above, we characterized the effects of
972 gene inactivation on tumorigenesis in terms of the number of tumors and total neoplastic cell
973 number ("tumor burden") associated with each genotype. Unlike the aforementioned metrics of
974 tumor size, tumor number and burden are linearly affected by lentiviral titer and are thus
975 sensitive to underlying differences in the representation of each Lenti-sgRNA/Cre vector in the
976 viral pool. Critically, each Tuba-seq experiment included a cohort of *KT* control mice. *KT* mice
977 lack expression of Cas9, thus all Lenti-sgRNA/Cre vectors are functionally equivalent in these
978 mice, and the observed tumor number and burden associated with each sgRNA reflects the
979 make-up of the viral pool.

980 To assess the extent to which a given gene (*X)* affects tumor number, we therefore first
981 normalized the number of sgX tumors in *KT;H11*$^{LSL\text{-}Cas9}$ mice (also *KT;p53*$^{flox/flox}$*;H11*$^{LSL\text{-}Cas9}$ and
982 *Braf*$^{LSL\text{-}V600E/+}$*T; H11*$^{LSL\text{-}Cas9}$ mice in the initial Kras-interacting protein screen and the paired
983 screen, respectively) to the number of sgX tumors in the *KT* mice:

984

985 $$Tumor\ number_{sgX} = \frac{Number\ of\ sgX\ tumors\ in\ KT; H11^{LSL-Cas9}\ mice}{Number\ of\ sgX\ tumors\ in\ KT\ mice}$$

986

987 As with the tumor size metrics, we then calculated a relative tumor number by normalizing this

988 statistic to the corresponding statistic calculated using sgInert tumors:

989

990 $$Relative\ tumor\ number_{sgX} = \frac{Tumor\ number_{sgX}}{Tumor\ number_{sgInert}}$$

991

992 Genes that influence relative tumor number modify the probability of tumor initiation

993 and/or the very early stages of oncogene-driven epithelial expansion, which prior work suggests

994 are imperfectly correlated with tumor growth at later stages. Relative tumor number thus

995 captures an additional and potentially important aspect of tumor suppressor gene function.

996

997 Analogous to the calculation of relative tumor number, we characterized the effect of each gene

998 on tumor burden by first normalizing the sgX tumor burden in Cas9-expressing mice to the

999 burden in KT mice:

1000

1001 $$Tumor\ burden_{sgX} = \frac{Total\ neoplastic\ cell\ number\ for\ sgX\ in\ KT; H11^{LSL-Cas9}\ mice}{Total\ neoplastic\ cell\ number\ for\ sgX\ in\ KT\ mice}$$

1002

1003 We then calculated a relative tumor burden by normalizing this number to the corresponding

1004 statistic calculated using sgInert tumors:

1005

1006 $$Relative\ tumor\ burden_{sgX} = \frac{Tumor\ burden_{sgX}}{Tumor\ burden_{sgInert}}$$

1007

1008 Tumor burden is an integration over tumor size and number, and thus reflects the total
1009 neoplastic load in each mouse. Tumor burden is thus more strongly related to morbidity than are
1010 our metrics of tumor size and is closely related to traditional measurements of tumor progression
1011 such as duration of survival and tumor area. While intuitively appealing, tumor burden is notably
1012 nosier than our metrics of tumor size as it is strongly determined by the size of the largest
1013 tumors.

1014

1015 *Calculation of confidence intervals and P-values for tumor growth and number metrics*

1016 Confidence intervals and *P*-values were calculated using bootstrap resampling to estimate
1017 the sampling distribution of each statistic. To account for both mouse-to-mouse variability and
1018 variability in tumor size and number within mice, we adopted a two-step, nested bootstrap
1019 approach where we first resampled mice, and then resampled tumors within each mouse in the
1020 pseudo-dataset. 10,000 bootstrap samples were drawn for all reported P-values. 95% confidence
1021 intervals were calculated using the 2.5th and 97.5th percentile of the bootstrapped statistics.
1022 Because we calculate metrics of tumor growth that are normalized to the same metrics in sgInert
1023 tumors, under the null model where genotype does not affect tumor growth, the test statistic is
1024 equal to 1. Two-sided p-values were thus calculated as followed:

1025 $$p = 2 * \min\{\Pr(T > 1), \Pr(T < 1)\}$$

1026 Where T is the test statistic and Pr(T>1) and Pr(T<1) were calculated empirically as the
1027 proportion of bootstrapped statistics that were more extreme than the baseline of 1. To account

1028 for multiple hypothesis testing, p-values were FDR-adjusted using the Benjamini-Hochberg
1029 procedure as implemented in the Python package stats models.
1030
1031 *AP-MS data visualization*
1032 AP-MS data was analyzed as described (Ding et al 2016). Briefly, protein spectral
1033 matches (PSMs; Kelly et al 2020) were normalized by protein length and total spectral matches
1034 per experiment. These normalized spectral abundance factors (NSAFs) were then normalized to
1035 NSAFs of matched prey proteins from a large cohort of unrelated AP/MS experiments to
1036 produce a Z-score. Z-scores are proportional to the areas of circles in bubble plots. In cluster
1037 diagrams, NSAFs are binarized by statistical significance (FDR > 0.5), similarities between
1038 interactome profiles are determined by cosine distance, and dendrogram topology is determined
1039 by UPGMA.
1040
1041
1042
1043
1044
1045
1046
1047
1048
1049
1050

ACKNOWLEDGEMNTS:

We thank the Stanford Veterinary Animal Care Staff for expert animal care, Human Pathology/Histology Service Center, Stanford Protein and Nucleic Acid Facility for experimental support; A. Orantes for administrative support; Members of the Winslow laboratory for helpful comments. R.T. was supported by a Stanford University School of Medicine Dean's Postdoctoral Fellowship, a Tobacco-Related Disease Research Program (TRDRP) Postdoctoral fellowship (27FT-0044), and a Stanford Cancer Institute fellowship. C.W.M. was supported by the NSF Graduate Research Fellowship Program and an Anne T. and Robert M. Bass Stanford Graduate Fellowship. J.D.H was supported by a Stanford University School of Medicine Dean's Postdoctoral Fellowship and a TRDRP Postdoctoral fellowship. H.C. was supported by a TRDRP Postdoctoral Fellowship (28FT-0019). This work was supported by NIH R01-CA207133 (to M.M.W and D.A.P.), NIH R01-CA231253 (to M.M.W and D.A.P), NIH R01-CA234349 (to M.M.W and D.A.P.), and in part by the Stanford Cancer institute support grant (NIH P30-CA124435).

1074

1075

1076

1077 **REFERENCES:**

1078 1. Karnoub AE, Weinberg RA. Ras oncogenes: split personalities. Nature reviews Molecular

1079 cell biology **2008**;9(7):517-31.

1080 2. Cox AD, Fesik SW, Kimmelman AC, Luo J, Der CJ. Drugging the undruggable RAS: mission

1081 possible? Nature reviews Drug discovery **2014**;13(11):828-51.

1082 3. Zhou B, Der CJ, Cox AD. The role of wild type RAS isoforms in cancer. 2016. Elsevier. p

1083 60-9.

1084 4. Wennerberg K, Rossman KL, Der CJ. The Ras superfamily at a glance. Journal of cell

1085 science **2005**;118(5):843-6.

1086 5. Hobbs GA, Der CJ, Rossman KL. RAS isoforms and mutations in cancer at a glance.

1087 Journal of cell science **2016**;129(7):1287-92.

1088 6. Stephen AG, Esposito D, Bagni RK, McCormick F. Dragging ras back in the ring. Cancer

1089 cell **2014**;25(3):272-81.

1090 7. Brose MS, Volpe P, Feldman M, Kumar M, Rishi I, Gerrero R*, et al.* BRAF and RAS

1091 mutations in human lung cancer and melanoma. Cancer research **2002**;62(23):6997-

1092 7000.

1093 8. Prior IA, Lewis PD, Mattos C. A comprehensive survey of Ras mutations in cancer. Cancer

1094 research **2012**;72(10):2457-67.

1095 9. Papke B, Der CJ. Drugging RAS: Know the enemy. Science **2017**;355(6330):1158-63.

1096 10. Keeton AB, Salter EA, Piazza GA. The RAS–effector interaction as a drug target. Cancer
1097 research **2017**;77(2):221-6.
1098 11. Zhou Y, Hancock JF. Deciphering lipid codes: K-Ras as a paradigm. Traffic
1099 **2018**;19(3):157-65.
1100 12. Wittinghofer A, Pal EF. The structure of Ras protein: a model for a universal molecular
1101 switch. Trends in biochemical sciences **1991**;16:382-7.
1102 13. Omerovic J, Hammond DE, Clague MJ, Prior IA. Ras isoform abundance and signalling in
1103 human cancer cell lines. Oncogene **2008**;27(19):2754-62.
1104 14. Kelly MR, Kostyrko K, Han K, Mooney NA, Jeng EE, Spees K*, et al.* Combined proteomic
1105 and genetic interaction mapping reveals new RAS effector pathways and susceptibilities.
1106 Cancer discovery **2020**;10(12):1950-67.
1107 15. Broyde J, Simpson DR, Murray D, Paull EO, Chu BW, Tagore S*, et al.* Oncoprotein-specific
1108 molecular interaction maps (SigMaps) for cancer network analyses. Nature
1109 biotechnology **2021**;39(2):215-24.
1110 16. Han K, Pierce SE, Li A, Spees K, Anderson GR, Seoane JA*, et al.* CRISPR screens in cancer
1111 spheroids identify 3D growth-specific vulnerabilities. Nature **2020**;580(7801):136-41.
1112 17. Cai H, Chew SK, Li C, Tsai MK, Andrejka L, Murray CW*, et al.* A functional taxonomy of
1113 tumor suppression in oncogenic KRAS-driven lung cancer. Cancer Discovery **2021**.
1114 18. Rogers ZN, McFarland CD, Winters IP, Seoane JA, Brady JJ, Yoon S*, et al.* Mapping the in
1115 vivo fitness landscape of lung adenocarcinoma tumor suppression in mice. Nature
1116 genetics **2018**;50(4):483-6.

1117 19. Rogers ZN, McFarland CD, Winters IP, Naranjo S, Chuang C-H, Petrov D*, et al.* A
1118 quantitative and multiplexed approach to uncover the fitness landscape of tumor
1119 suppression in vivo. Nature methods **2017**;14(7):737-42.
1120 20. Jackson EL, Willis N, Mercer K, Bronson RT, Crowley D, Montoya R*, et al.* Analysis of lung
1121 tumor initiation and progression using conditional expression of oncogenic K-ras. Genes
1122 & development **2001**;15(24):3243-8.
1123 21. Guerra C, Mijimolle N, Dhawahir A, Dubus P, Barradas M, Serrano M*, et al.* Tumor
1124 induction by an endogenous K-ras oncogene is highly dependent on cellular context.
1125 Cancer cell **2003**;4(2):111-20.
1126 22. Chuang C-H, Greenside PG, Rogers ZN, Brady JJ, Yang D, Ma RK*, et al.* Molecular
1127 definition of a metastatic lung cancer state reveals a targetable CD109–Janus kinase–
1128 Stat axis. Nature medicine **2017**;23(3):291-300.
1129 23. Ruiz S, Santos E, Bustelo XR. RasGRF2, a guanosine nucleotide exchange factor for Ras
1130 GTPases, participates in T-cell signaling responses. Molecular and cellular biology
1131 **2007**;27(23):8127-42.
1132 24. Takaya A, Kamio T, Masuda M, Mochizuki N, Sawa H, Sato M*, et al.* R-Ras regulates
1133 exocytosis by Rgl2/Rlf-mediated activation of RalA on endosomes. Molecular biology of
1134 the cell **2007**;18(5):1850-60.
1135 25. Zhang FL, Kirschmeier P, Carr D, James L, Bond RW, Wang L*, et al.* Characterization of
1136 Ha-ras, N-ras, Ki-Ras4A, and Ki-Ras4B as in vitro substrates for farnesyl protein
1137 transferase and geranylgeranyl protein transferase type I. Journal of Biological
1138 Chemistry **1997**;272(15):10232-9.

1139 26. Marais R, Light Y, Paterson H, Marshall C. Ras recruits Raf-1 to the plasma membrane
1140 for activation by tyrosine phosphorylation. The EMBO journal **1995**;14(13):3136-45.
1141 27. Kohl NE, Mosser SD, DeSolms SJ, Giuliani EA, Pompliano DL, Graham SL*, et al.* Selective
1142 inhibition of ras-dependent transformation by a farnesyltransferase inhibitor. Science
1143 **1993**;260(5116):1934-7.
1144 28. Rowinsky EK, Windle JJ, Von Hoff DD. Ras protein farnesyltransferase: a strategic target
1145 for anticancer therapeutic development. Journal of Clinical Oncology **1999**;17(11):3631-
1146 52.
1147 29. Collisson E, Campbell J, Brooks A, Berger A, Lee W, Chmielecki J*, et al.* Comprehensive
1148 molecular profiling of lung adenocarcinoma: The cancer genome atlas research network.
1149 Nature **2014**;511(7511):543-50.
1150 30. Murray CW, Brady JJ, Tsai MK, Li C, Winters IP, Tang R*, et al.* An LKB1–SIK axis
1151 suppresses lung tumor growth and controls differentiation. Cancer discovery
1152 **2019**;9(11):1590-605.
1153 31. Staffas A, Karlsson C, Persson M, Palmqvist L, Bergo M. Wild-type KRAS inhibits
1154 oncogenic KRAS-induced T-ALL in mice. Leukemia **2015**;29(5):1032-40.
1155 32. Ambrogio C, Köhler J, Zhou Z-W, Wang H, Paranal R, Li J*, et al.* KRAS dimerization
1156 impacts MEK inhibitor sensitivity and oncogenic activity of mutant KRAS. Cell
1157 **2018**;172(4):857-68. e15.
1158 33. Kong G, Chang Y-I, Damnernsawad A, You X, Du J, Ranheim EA*, et al.* Loss of wild-type
1159 Kras promotes activation of all Ras isoforms in oncogenic Kras-induced leukemogenesis.
1160 Leukemia **2016**;30(7):1542-51.

1161 34. Young A, Lou D, McCormick F. Oncogenic and wild-type Ras play divergent roles in the
1162 regulation of mitogen-activated protein kinase signaling. Cancer discovery
1163 **2013**;3(1):112-23.
1164 35. Grabocka E, Pylayeva-Gupta Y, Jones MJ, Lubkov V, Yemanaberhan E, Taylor L*, et al.*
1165 Wild-type H-and N-Ras promote mutant K-Ras-driven tumorigenesis by modulating the
1166 DNA damage response. Cancer cell **2014**;25(2):243-56.
1167 36. Zhou Y, Liang H, Rodkey T, Ariotti N, Parton RG, Hancock JF. Signal integration by lipid-
1168 mediated spatial cross talk between Ras nanoclusters. Molecular and cellular biology
1169 **2014**;34(5):862-76.
1170 37. Zhou Y, Hancock JF. Ras nanoclusters: Versatile lipid-based signaling platforms.
1171 Biochimica et Biophysica Acta (BBA)-Molecular Cell Research **2015**;1853(4):841-9.
1172 38. Henis YI, Hancock JF, Prior IA. Ras acylation, compartmentalization and signaling
1173 nanoclusters. Molecular membrane biology **2009**;26(1-2):80-92.
1174 39. Inouye K, Mizutani S, Koide H, Kaziro Y. Formation of the Ras dimer is essential for Raf-1
1175 activation. Journal of Biological Chemistry **2000**;275(6):3737-40.
1176 40. Muratcioglu S, Chavan TS, Freed BC, Jang H, Khavrutskii L, Freed RN*, et al.* GTP-
1177 dependent K-Ras dimerization. Structure **2015**;23(7):1325-35.
1178 41. Lin W-C, Iversen L, Tu H-L, Rhodes C, Christensen SM, Iwig JS*, et al.* H-Ras forms dimers
1179 on membrane surfaces via a protein–protein interface. Proceedings of the National
1180 Academy of Sciences **2014**;111(8):2996-3001.
1181 42. Güldenhaupt J, Rudack T, Bachler P, Mann D, Triola G, Waldmann H*, et al.* N-Ras forms
1182 dimers at POPC membranes. Biophysical journal **2012**;103(7):1585-93.

1183 43. Li Y-C, Lytle NK, Gammon ST, Wang L, Hayes TK, Sutton MN*, et al.* Analysis of RAS
1184 protein interactions in living cells reveals a mechanism for pan-RAS depletion by
1185 membrane-targeted RAS binders. Proceedings of the National Academy of Sciences
1186 **2020**;117(22):12121-30.
1187 44. Dankort D, Filenova E, Collado M, Serrano M, Jones K, McMahon M. A new mouse
1188 model to explore the initiation, progression, and therapy of BRAFV600E-induced lung
1189 tumors. Genes & development **2007**;21(4):379-84.
1190 45. Dietrich P, Gaza A, Wormser L, Fritz V, Hellerbrand C, Bosserhoff AK. Neuroblastoma RAS
1191 viral oncogene homolog (NRAS) is a novel prognostic marker and contributes to
1192 sorafenib resistance in hepatocellular carcinoma. Neoplasia **2019**;21(3):257-68.
1193 46. Weyandt JD, Lampson BL, Tang S, Mastrodomenico M, Cardona DM, Counter CM. Wild-
1194 type Hras suppresses the earliest stages of tumorigenesis in a genetically engineered
1195 mouse model of pancreatic cancer. PloS one **2015**;10(10):e0140253.
1196 47. Jeng H-H, Taylor LJ, Bar-Sagi D. Sos-mediated cross-activation of wild-type Ras by
1197 oncogenic Ras is essential for tumorigenesis. Nature communications **2012**;3(1):1-8.
1198 48. Miller MS, Miller LD. RAS mutations and oncogenesis: not all RAS mutations are created
1199 equally. Frontiers in genetics **2012**;2:100.
1200

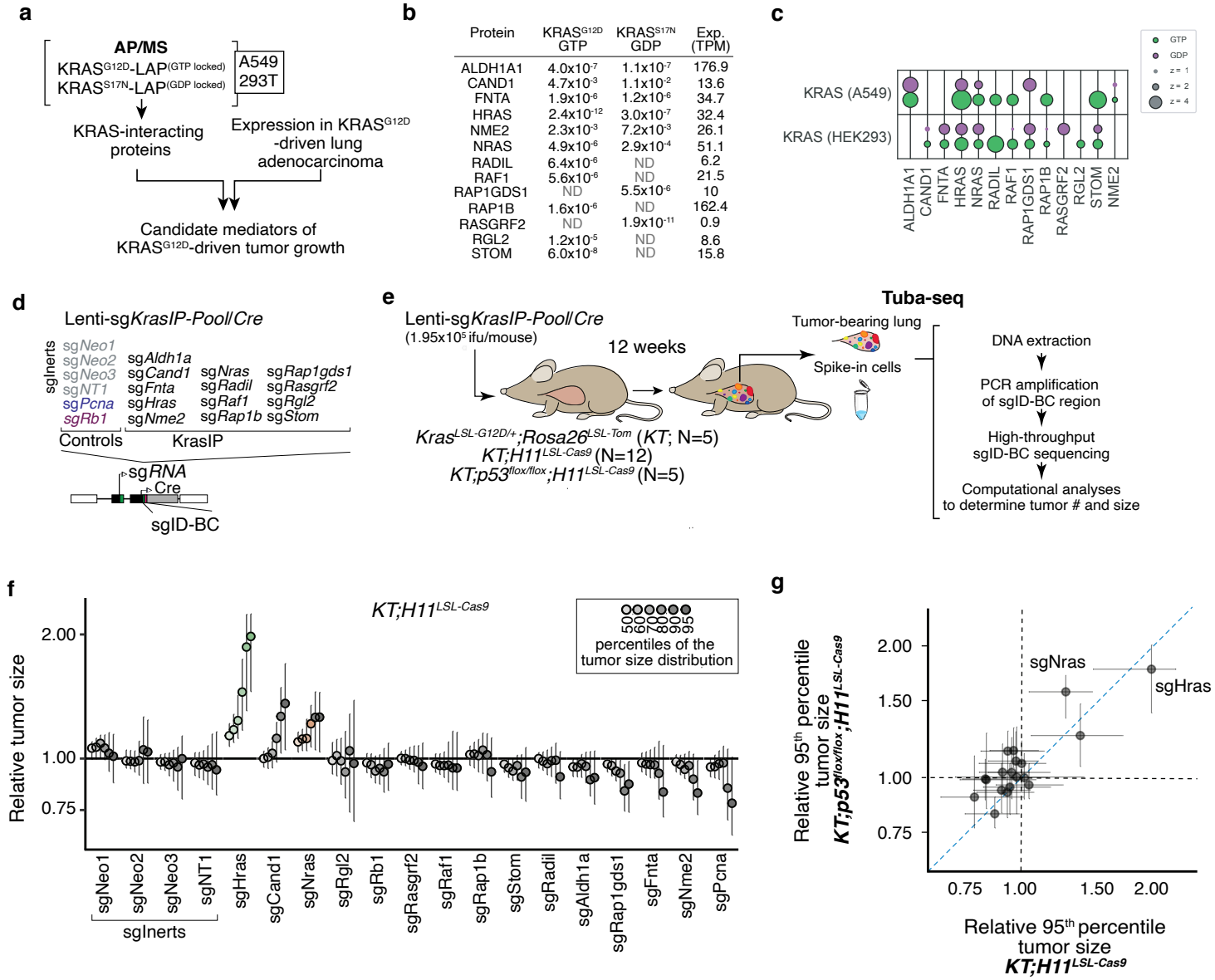

Protein	KRAS^{G12D} GTP	KRAS^{S17N} GDP	Exp. (TPM)
ALDH1A1	4.0×10^{-7}	1.1×10^{-7}	176.9
CAND1	4.7×10^{-3}	1.1×10^{-2}	13.6
FNTA	1.9×10^{-6}	1.2×10^{-6}	34.7
HRAS	2.4×10^{-12}	3.0×10^{-7}	32.4
NME2	2.3×10^{-3}	7.2×10^{-3}	26.1
NRAS	4.9×10^{-6}	2.9×10^{-4}	51.1
RADIL	6.4×10^{-6}	ND	6.2
RAF1	5.6×10^{-6}	ND	21.5
RAP1GDS1	ND	5.5×10^{-6}	10
RAP1B	1.6×10^{-6}	ND	162.4
RASGRF2	ND	1.9×10^{-11}	0.9
RGL2	1.2×10^{-5}	ND	8.6
STOM	6.0×10^{-8}	ND	15.8

Figure 1. Multiplexed identification of KRAS-interacting proteins that impact KRAS^{G12D}-driven lung cancer growth *in vivo*.

a. Candidate mediators of KRAS-driven lung tumor growth were identified on the basis of their interactions with GTP- and GDP-locked Kras in multiple AP/MS-based protein-protein interaction screens and their expression in a mouse model of Kras-driven lung adenocarcinoma.

b. Selected KRAS-interacting proteins interact with either GTP- or GDP-locked KRAS (shown as NSAF in A549 cells) and their homolog is expressed in KRAS^{G12D}-driven lung cancer (shown as TPM).

c. Bubble plot of two AP/MS experiments with GTP- and GDP-locked mutant GTPases as baits (rows), showing the enrichment of selected candidate KRAS-interacting proteins (columns). Dark borders indicate FDR < 0.05.

d. Schematic of tumor initiation with a pool of barcoded Lenti-sgRNA/Cre vectors (Lenti-sgKrasIP-Pool/Cre). The lentiviral pool includes four Inert sgRNAs that are either non-targeting (NT) or target a functionally inert locus (Neo1-3, targeting NeoR in the *R26*$^{LSL\text{-}tdTomato}$ allele). Each barcoded lentiviral vector contains an sgRNA, Cre, and a two-component barcode composed of an sgRNA identifier (sgID) and a random barcode (BC). This design allows inactivation of multiple target genes in parallel followed by quantification of the resulting tumor size distributions through high-throughput sgID-BC sequencing.

e. Tumors were initiated in cohorts of *KT*, *KT;H11*$^{LSL\text{-}Cas9}$ and *KT;p53*$^{flox/flox}$*;H11*$^{LSL\text{-}Cas9}$ mice through intratracheal delivery of Lenti-sgKrasIP-Pool/Cre. Tuba-seq was performed on each tumor-bearing lung 12 weeks after initiation, followed by analyses of sgID-BC sequencing data to characterize the effects of inactivating each gene.

f. Tumor sizes at indicated percentiles for each sgRNA relative to the size of sgInert-containing tumors at the corresponding percentiles in *KT;H11*$^{LSL\text{-}Cas9}$ mice. Genes are ordered by 95th percentile tumor size, with sgInerts on the left. sgInerts are in gray, and the line at y=1 indicates no effect relative to sgInert. Error bars indicate 95% confidence intervals. Percentiles that are signficantly different from sgInert (two-sided FDR-adjusted $p < 0.05$) are in color. Confidence intervals and P-values were calculated by bootstrap resampling.

g. Comparison of 95th percentile tumor size for each sgRNA relative to the size the 95th percentile tumor size of sgInert-containing tumors in *KT;H11*$^{LSL\text{-}Cas9}$ mice versus *KT;p53*$^{flox/flox}$*;H11*$^{LSL\text{-}Cas9}$ mice. Error bars indicate 95% confidence intervals calculated by bootstrap resampling.

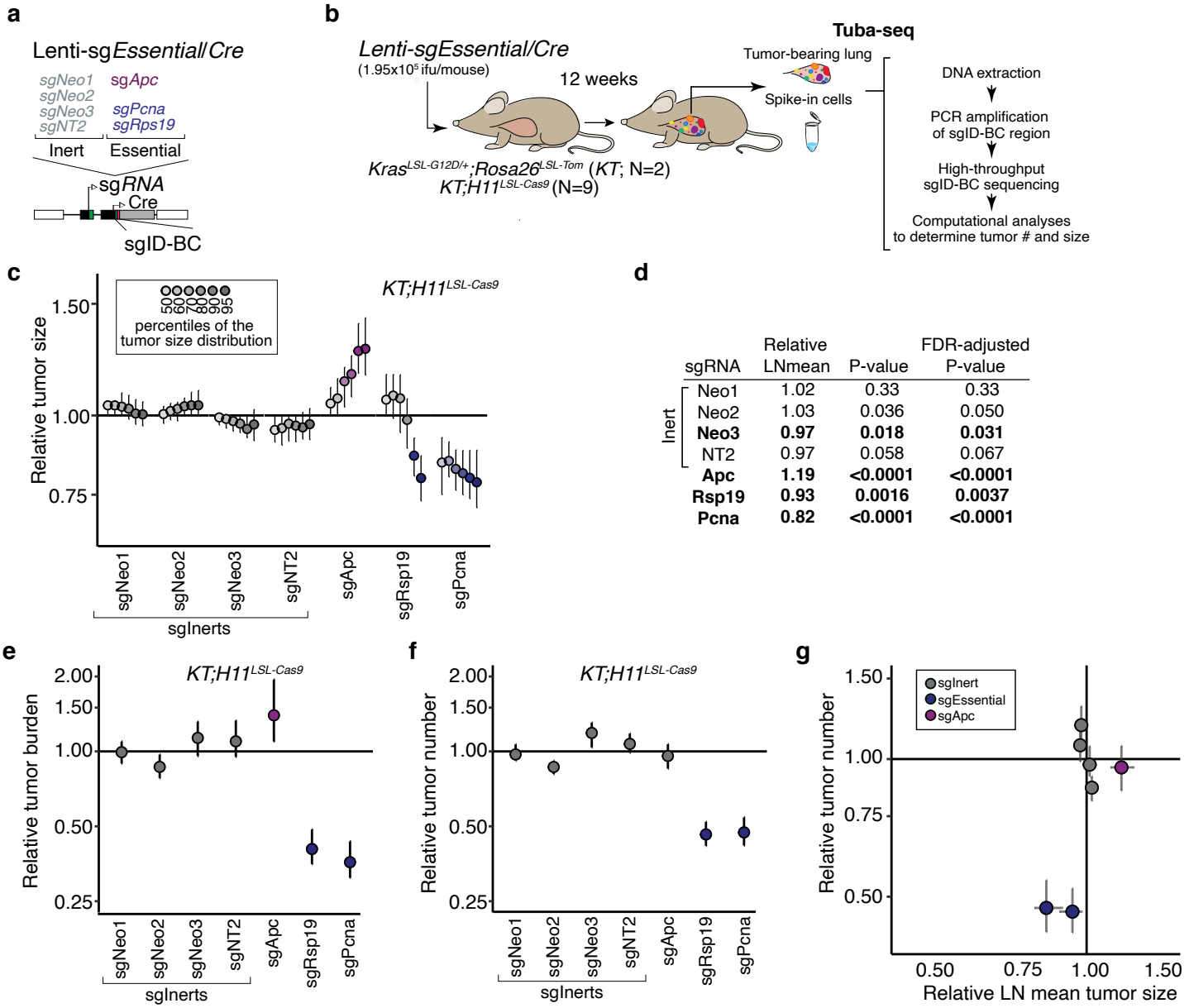

	sgRNA	Relative LNmean	P-value	FDR-adjusted P-value
Inert	Neo1	1.02	0.33	0.33
Inert	Neo2	1.03	0.036	0.050
Inert	**Neo3**	**0.97**	**0.018**	**0.031**
Inert	NT2	0.97	0.058	0.067
	Apc	**1.19**	**<0.0001**	**<0.0001**
	Rsp19	**0.93**	**0.0016**	**0.0037**
	Pcna	**0.82**	**<0.0001**	**<0.0001**

Supplemental Figure 1. Tumor barcoding coupled with barcode sequencing (Tuba-seq) can uncover engineered alterations that reduce tumor number and growth.

a-b. Schematic of the Tuba-seq approach to measure the effects of essential gene inactivation on tumor growth. Lentiviral-sgRNA/Cre vectors with inert sgRNAs (gray) or sgRNAs targeting known essential genes (navy) were diversified with a two component sgID-BC. A vector targeting known tumor suppressor *Apc* was included as a positive control (**a**). Tumors were initiated with this barcoded Lenti-sgEssential/Cre pool in KT and KT;H11$^{LSL\text{-}Cas9}$ mice. Tuba-seq was performed on each tumor-bearing lung 12 weeks after initiation, followed by analyses of sgID-BC sequencing data to characterize the effects of inactivating each gene (**b**).

c. Tumor sizes at indicated percentiles for each sgRNA relative to the size of sgInert-containing tumors at the corresponding percentiles. Line at y=1 indicates no effect relative to sgInert. Error bars indicate 95% confidence intervals. Percentiles that are signficantly different from sgInert (two-sided FDR-corrected $p < 0.05$) are in color. Confidence intervals and P-values were calculated by bootstrap resampling.

d. The impact of each sgRNA on mean tumor size relative to sgInerts, assuming a log-normal distribution of tumor sizes (LNmean). sgRNAs with two-sided P<0.05 after FDR-adjustment are in bold.

e. The impact of each sgRNA on tumor burden (number of neoplastic cells aggregated across all tumors of a genotype) relative to sgInerts and normalized to the same statistic in *KT* mice to account for representation of each sgRNA in the viral pool. sg*Inert*s are in gray and the line at y=1 indicates no effect. Error bars indicate 95% confidence intervals. Relative burdens significantly different from sgInert (two-sided FDR-corrected p<0.05) are in color. Confidence intervals and P-values were calculated by bootstrap resampling.

f. The impact of each sgRNA on tumor number relative to sgInerts and normalized to the same statistic in *KT* mice to account for representation of each sgRNA in the viral pool. sg*Inert*s are in gray and the line at y=1 indicates no effect. Error bars indicate 95% confidence intervals. Relative tumor numbers significantly different from sgInert (two-sided FDR-corrected p<0.05) are in color. Confidence intervals and P-values were calculated by bootstrap resampling.

g. The impact of each sgRNA on tumor number plotted against its impact on LNmean tumor size. The lines at y=1 and x=1 indicate no effect relative to sgInert on tumor number and size, respectively. sgRsp19 and sgPcna cluster in the lower left quadrant near x=1, indicating that targeting essential genes strongly reduces tumor number but only moderately decreases average tumor size. Error bars indicate 95% confidence intervals calculated by bootstrap resampling.

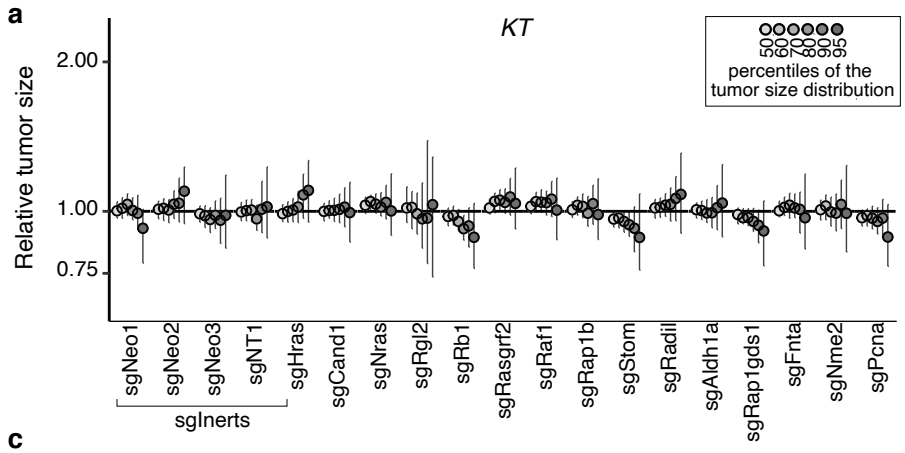

b

	sgRNA	Relative LNmean	P-value	FDR-adjusted P-value
Inert	Neo1	1.03	0.26	0.46
	Neo2	1.03	0.64	0.77
	Neo3	0.98	0.53	0.72
	NT1	0.95	0.32	0.46
	Hras	**1.52**	**<0.0001**	**<0.0001**
	Cand1	1.15	0.039	0.12
	Nras	**1.19**	**0.0014**	**0.013**
	Rgl2	1.01	0.94	0.94
	Rb1	0.96	0.27	0.46
	Rasgrf2	0.99	0.69	0.77
	Raf1	0.98	0.69	0.77
	Rap1b	0.99	0.93	0.94
	Stom	0.94	0.055	0.14
	Radil	0.97	0.29	0.46
	Aldh1a	0.94	0.060	0.14
	Rap1gds1	**0.90**	**0.003**	**0.019**
	Fnta	0.92	0.11	0.23
	Nme2	0.91	0.037	0.12
	Pcna	0.89	0.035	0.12

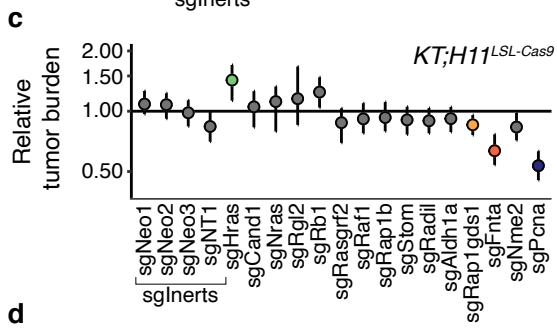

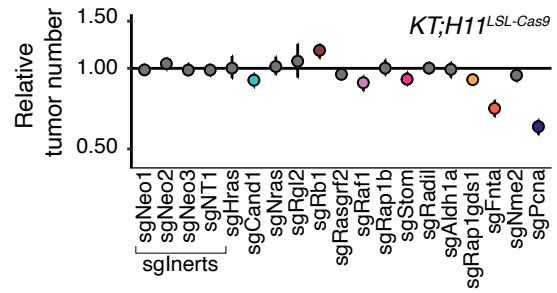

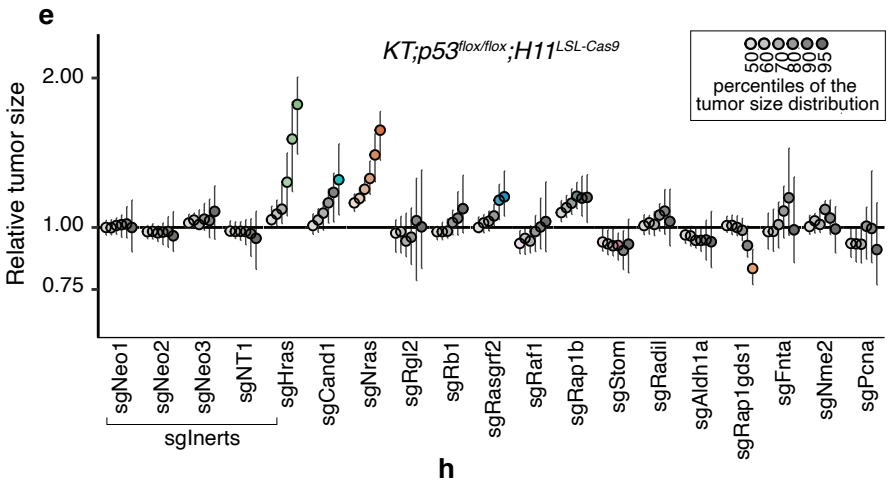

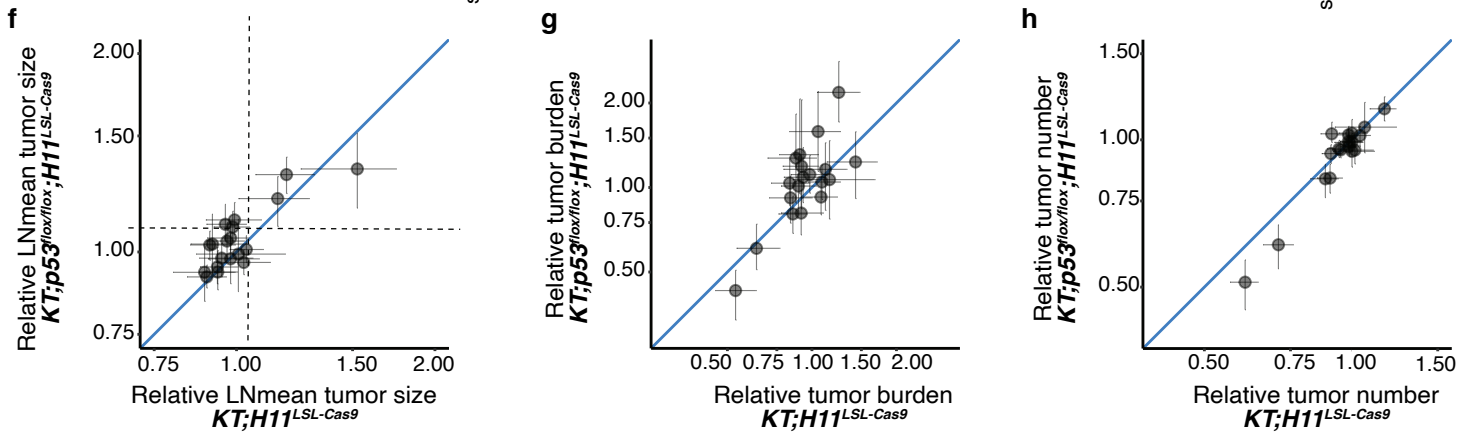

Supplemental Figure 2. Inactivation of KRAS-interacting proteins has similar impacts on tumor growth in p53-proficient and p53-deficient contexts.
a. Tumor sizes at indicated percentiles for each sgRNA relative to the size of sgInert-containing tumors at the corresponding percentiles in *KT* mice. *KT* mice lack Cas9, thus all sgRNAs are functionally equivalent to sgInerts. Genes are ordered as in Figure 1f. Line at y=1 indicates no effect relative to sgInert. Error bars indicate 95% confidence intervals. Confidence intervals and P-values were calculated by bootstrap resampling. As expected, no percentiles were signficantly different from sgInert (two-sided FDR-adjusted $p < 0.05$).
b. The impact of each sgRNA on mean tumor size relative to sgInerts in *KT;H11*$^{LSL\text{-}Cas9}$, assuming a log-normal distribution of tumor sizes (LNmean). sgRNAs with two-sided P<0.05 after FDR-adjustment are in bold. P-values were calculated by bootstrap resampling.
c-d. The impact of each sgRNA on tumor burden (**c**) and number (**d**) relative to sgInerts in *KT;H11*$^{LSL\text{-}Cas9}$mice, normalized to the corresponding statistic in *KT* mice to account for representation of each sgRNA in the viral pool. sgInerts are in gray and the line at y=1 indicates no effect. Error bars indicate 95% confidence intervals. Relative tumor burdens and numbers significantly different from sgInert (two-sided FDR-adjusted p<0.05) are in color. Confidence intervals and P-values were calculated by bootstrap resampling.
e. Tumor sizes at the indicated percentiles for each sgRNA relative to the size of sgInert-containing tumors in KT;p53$^{flox/flox}$;H11$^{LSL\text{-}Cas9}$ mice. Genes are ordered as in Figure 1f. Dashed line indicates no effect relative to sgInert. Error bars indicate 95% confidence intervals. Percentiles that are signficantly different from sgInert (two-sided FDR-adjusted $p < 0.05$) are in color. Confidence intervals and P-values calculated by bootstrap resampling.
f-h. Comparison of the impact of each sgRNA on relative LNmean tumor size (**f**), tumor burden (**g**) and tumor number (**h**) in *KT;H11*$^{LSL\text{-}Cas9}$and *KT;p53*$^{flox/flox}$*KT;H11*$^{LSL\text{-}Cas9}$*;H11*$^{LSL\text{-}Cas9}$ mice. Error bars indicate 95% confidence intervals calculated by bootstrap resampling.

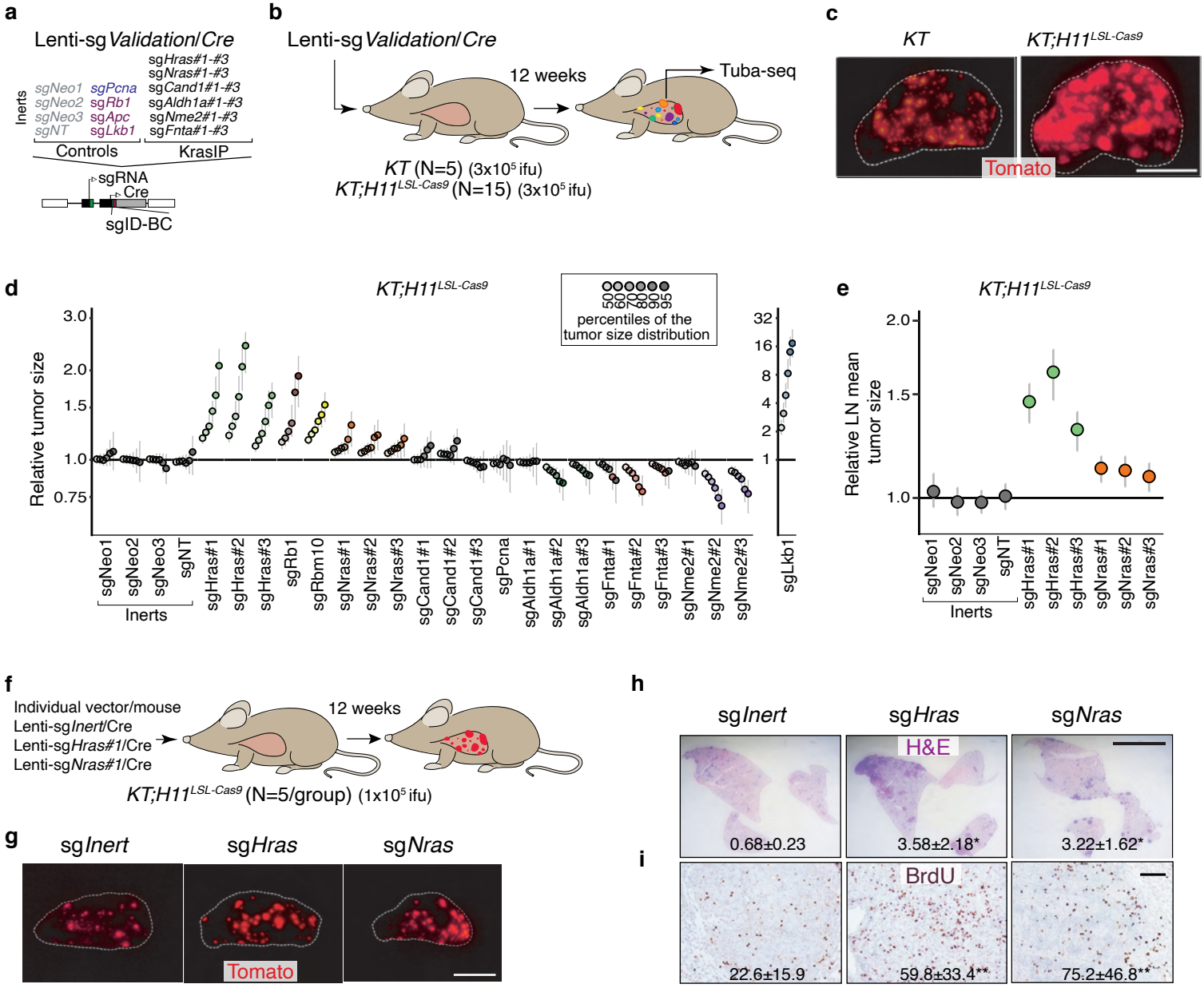

Figure 2. HRAS and NRAS are potent suppressors of KRAS^{G12D}-driven lung cancer growth *in vivo*

a,b. A pool of barcoded Lenti-sgRNA/Cre vectors (Lenti-sgValidation/Cre) targeting candidate mediators of KRAS-driven lung tumor growth identified in the initial KRAS-interacting protein Tuba-seq screen was used to initiate tumors in validation cohorts of *KT* and *KT;H11$^{LSL\text{-}Cas9}$* mice. This lentiviral pool includes four Inert sgRNAs, as well as sgRNAs targeting *Lkb1*, *Rb1*, and *Rbm10* as tumor suppressor controls. Each candidate gene from the initial screen is targeted with three sgRNAs. Tumors were initiated throuh intratracheal delivery of Lenti-sgValidation/Cre, and Tuba-seq was performed on each tumor-bearing lung 12 weeks after initiation, followed by analyses of sgID-BC sequencing data to characterize the effects of inactivating each gene (**b**).

c. Fluorescence images of representative lung lobes 12 weeks after tumor initiation. Scale bars = 5 mm. Lung lobes are outlined with a white dashed line.

d. Tumor sizes at indicated percentiles for each sgRNA relative to the size of sgInert-containing tumors at the corresponding percentiles in *KT;H11$^{LSL\text{-}Cas9}$* mice. Genes are ordered by 95th percentile tumor size, with sgInerts on the left. Note that sgLkb1 is plotted on a separate scale to facilitate visualization of sgRNAs with lesser magnitudes of effect. Dashed line indicates no effect relative to sgInert. Error bars indicate 95% confidence intervals. 95% confidence intervals and P-values were calculated by bootstrap resampling. Percentiles that are signficantly different from sgInert (2-sided FDR-adjusted $p < 0.05$) are in color.

e. Targeting Hras and Nras significantly increases mean tumor size relative to sgInerts, assuming a log-normal distribution of tumor sizes (LNmean). Error bars indicate 95% confidence intervals calculated by bootstrap resampling.

f. Schematic of tumor initiation with individual Lenti-sgRNA/Cre vectors. Mouse number and titer of the lentiviral vectors are indicated.

g. Representative fluorescence images of lungs from *KT;H11$^{LSL\text{-}Cas9}$* mice after tumor initiation with Lenti-sgRNA/Cre vectors as indicated. Scale bar = 5 mm.

h. Representative H&E images of lungs from *KT;H11$^{LSL\text{-}Cas9}$* mice after tumor initiation with Lenti-sgRNA/Cre vectors as indicated. Tumor area (percentage of total lung area) from each mouse is shown as Mean ± SD. *: $p<0.05$; Scale bar = 5 mm.

i. Representative BrdU staining images of lungs from *KT;H11$^{LSL\text{-}Cas9}$* mice after tumor initiation with Lenti-sgRNA/Cre vectors as indicated. Number of Brdu^{+} cells per field is shown as Mean ± SD. **: $p<0.01$; Scale bar = 100 μm.

a

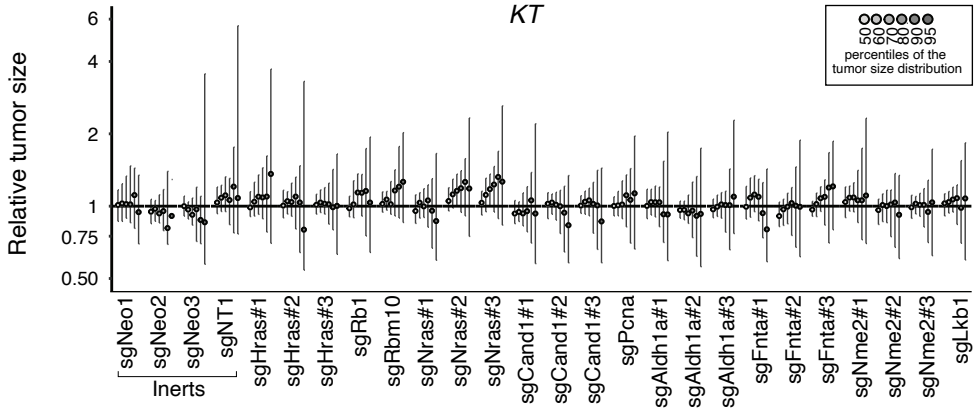

b

	sgRNA	Relative LNmean	P-value	FDR-adjusted P-value
Inert	Neo1	1.03	0.45	0.51
	Neo2	0.98	0.57	0.59
	Neo3	0.98	0.43	0.51
	NT1	1.01	0.82	0.82
	Lkb1	**8.85**	**<0.001**	**<0.001**
	Hras#1	**1.31**	**<0.001**	**<0.001**
	Hras#2	**1.46**	**<0.001**	**<0.001**
	Hras#3	**1.64**	**<0.001**	**<0.001**
	Rb1	**1.41**	**<0.001**	**<0.001**
	Rbm10	**1.31**	**<0.001**	**<0.001**
	Nras#1	**1.09**	**0.0050**	**0.0090**
	Nras#2	**1.11**	**0.0014**	**0.0028**
	Nras#3	**1.12**	**<0.001**	**<0.001**
	Cand1#1	1.06	0.038	0.059
	Cand1#2	0.97	0.16	0.23
	Cand1#3	1.03	0.48	0.52
	Pcna	0.96	0.38	0.46
	Aldh1a#1	0.96	0.25	0.34
	Aldh1a#2	0.93	**0.0052**	**0.0090**
	Aldh1a#3	0.90	**<0.001**	**<0.001**
	Fnta#1	0.93	**<0.001**	**<0.001**
	Fnta#2	0.92	**0.017**	**0.027**
	Fnta#3	0.87	**<0.001**	**<0.001**
	Nme2#1	0.82	**<0.001**	**<0.001**
	Nme2#2	0.86	**<0.001**	**<0.001**
	Nme2#3	0.98	0.33	0.43

c

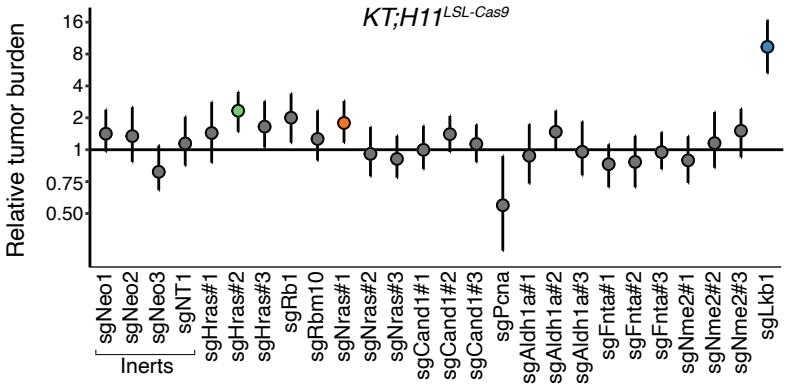

d

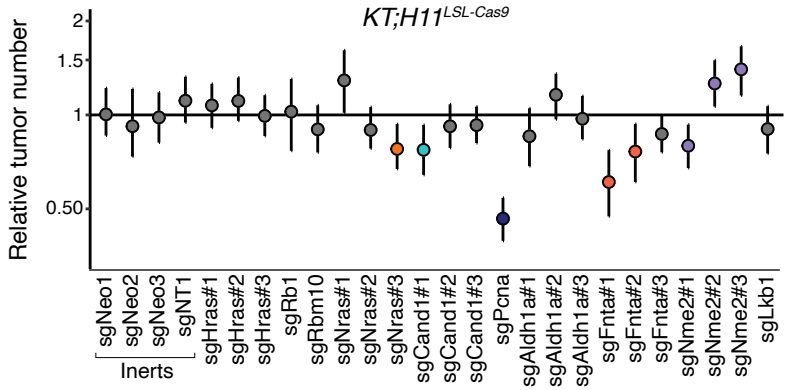

Supplemental Figure 3. Top candidate KRAS-interacting proteins from initial Tuba-seq screen impact multiple metrics of tumor growth in validation cohort.

a. Tumor sizes at indicated percentiles for each sgRNA relative to the size of sgInert-containing tumors at the corresponding percentiles in *KT* mice. *KT* mice lack Cas9, thus all sgRNAs are functionally equivalent to sgInerts. Genes are ordered as in Figure 2d, but note the change in axis scaling. Line at y=1 indicates no effect relative to sgInerts. Error bars indicate 95% confidence intervals. Confidence intervals and P-values were calculated by bootstrap resampling. As expected, no percentiles were signficantly different from sgInert (FDR-adjusted $p < 0.05$).

b. The impact of each sgRNA on mean tumor size relative to sgInerts, assuming a log-normal distribution of tumor sizes (LNmean). Two-sided P-values were calculated by bootstrap resampling. sgRNAs with P<0.05 after FDR-adjustment are in bold. Note that this data for the sgInerts, sgHras#1-3 and sgNras#1-3 is also plotted in Figure 2e.

c. The impact of each sgRNA on tumor burden relative to sgInerts in *KT;H11*$^{LSL\text{-}Cas9}$ mice, normalized to the corresponding statistic in *KT* mice to account for representation of each sgRNA in the viral pool. sgInerts are in gray and the line at y=1 indicates no effect. Error bars indicate 95% confidence intervals. Relative tumor burdens significantly different from sgInert (two-sided FDR-adjusted p<0.05) are in color. Confidence intervals and P-values were calculated by bootstrap resampling.

d. The impact of each sgRNA on tumor number relative to sgInerts in *KT;H11*$^{LSL\text{-}Cas9}$ mice, normalized to the corresponding statistic in KT mice to account for representation of each sgRNA in the viral pool. sgInerts are in gray and the line at y=1 indicates no effect. Error bars indicate 95% confidence intervals. Relative tumor numbers significantly different from sgInert (two-sided FDR-adjusted p<0.05) are in color. Confidence intervals and P-values were calculated by bootstrap resampling.

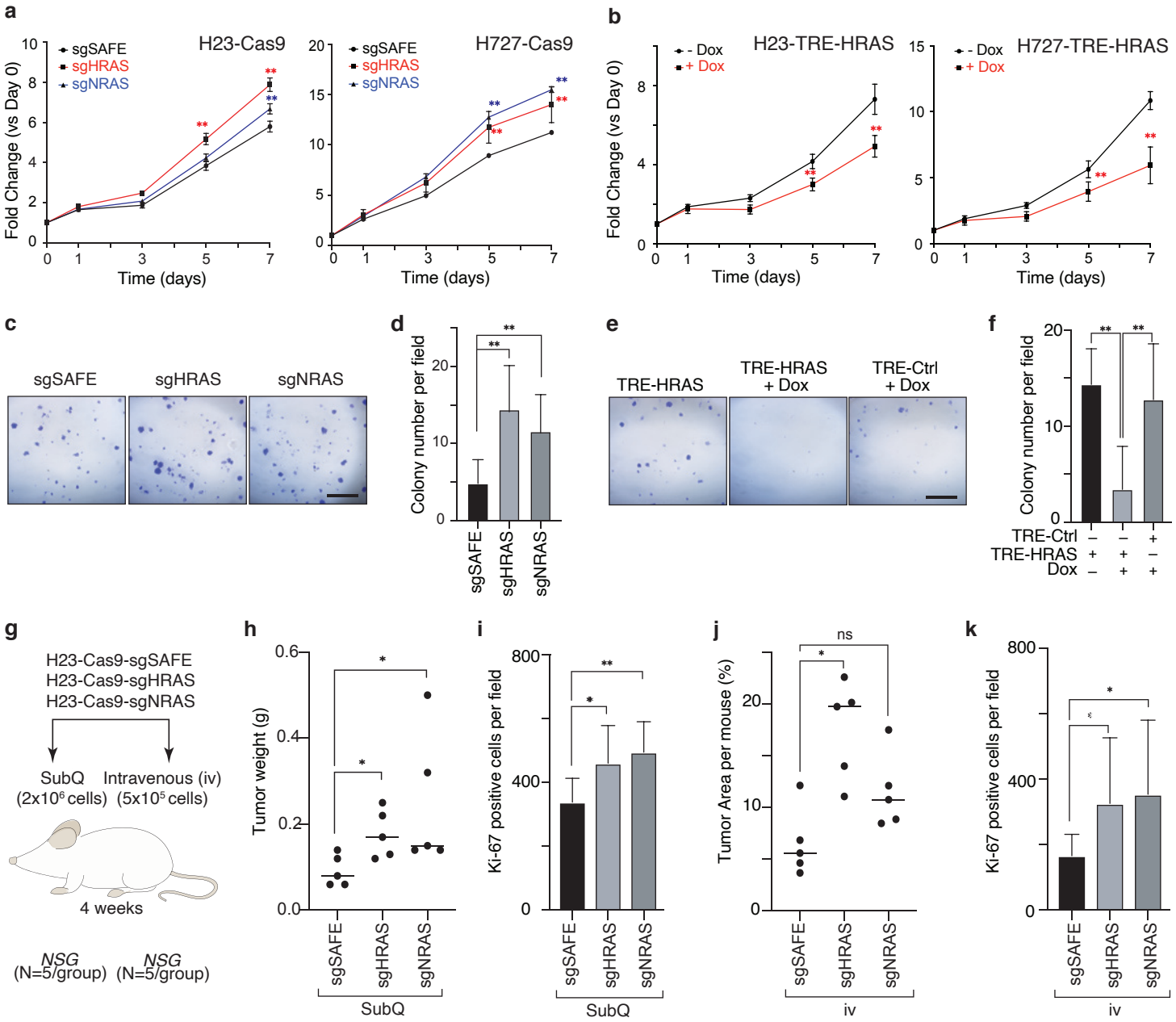

Figure 3. Wildtype HRAS or NRAS constrain the growth of human KRAS-driven cancer cell lines.

a. Inactivation of wild type HRAS or NRAS increases growth of KRAS-mutant H23 (G12C) and H727 (G12V) cells. Wildtype (sgSAFE) or HRAS- or NRAS-knockout cells were seeded in 96 well plates and cultured under limited serum (1%). Cell numbers were measured via CCK8 assay. Points are Mean±SD of 12 wells normalized to Day 0. **: $p<0.01$

b. Re-expression of wild type HRAS suppresses proliferation of HRAS-null H23 and H727 cells. TRE-HRAS cells were seeded in 96 well plates and cultured under limited serum (1%) with or without 50 ng/ml Doxycycline (Dox) and cell numbers were measured via CCK8 assay. Points are Mean±SD of 12 wells normalized to Day 0. **: $p<0.01$

c-d. Inactivation of HRAS or NRAS increases H23 colony formation. Wildtype (sgSAFE), HRAS-knockout (sgHRAS), or NRAS-knockout (sgNRAS) H23 cells were seeded at 1000 cells/well in 6-well plates and grown for two weeks. Cells were stained with crystal violet. **c**. Representative images. Scale bar = 5mm. **d**. Mean±SD of colony number of 12 fields. **: $p<0.01$

e-f. Re-expression of wild type HRAS suppresses HRAS-null H23 cell colony formation. TRE-Ctrl or TRE-HRAS H23 cells were seeded at 1000 cells/well in 6-well plates and grown with or without 50 ng/ml Doxycycline (Dox) for two weeks. Cells were stained with crystal violet. **e**. Representative images. Scale bar = 5mm. **f**. Mean±SD of colony number of 12 fields. **: $p<0.01$

g-k. Inactivation of wild type HRAS or NRAS increases H23 cell growth after transplantation. **g.** Schematic of tumor initiation with subcutaneous (SubQ) or intravenous (IV) transplantation of H23 cells with inactivation of HRAS or NRAS in NSG mice. Mouse number, cell number, and tumor growth time after transplantation are indicated. **h**. Tumor weight from SubQ transplantation of indicated cells. Each dot represents a mouse. Mean value was shown. **i**. Ki67^{pos} cell number in tumor section from SubQ transplantation of indicated cells was shown as Mean±SD value of 20 view fields. **j**. Tumor area (percentage of h-mitochondria^{pos} area) from IV transplantation of indicated cells. Each dot represents a tumor. Mean value was shown. **k**. Ki67^{pos} cell number in tumor section from IV transplantation of indicated cells is shown as Mean±SD value of 20 view fields (200x). *: $p<0.05$; **: $p<0.01$; ns: not significant.

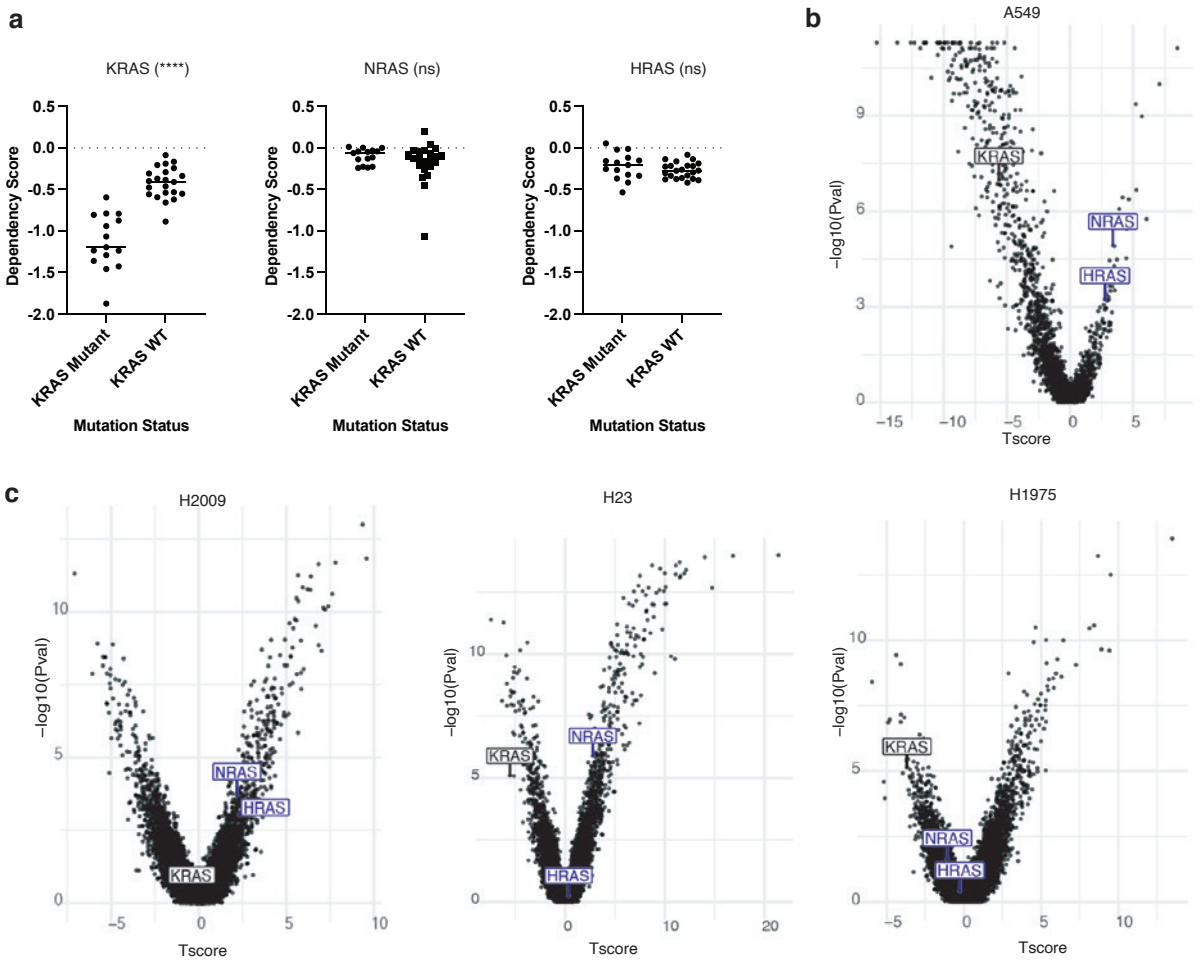

Supplemental Figure 4. Dependency of RAS family member across human LUAD cell lines.

a. Distribution of dependency scores for each RAS family member across human LUAD cell lines divided by KRAS mutation status. **** ($p < 0.0001$), ns (not-significant).

b. Volcano plot showing effects of RAS gene knockouts in A549 cells. (Data source: Marcus Robert Kelly, Kaja Kostyrko, Kyuho Han, et al. 2020)

c. Volcano plot showing effects of RAS gene knockouts in KRAS-mutant human LUAD cells (left: H2009, mid: H23, right: H1975) in 3D culture. (Data source: Kyuho Han, et al. 2020)

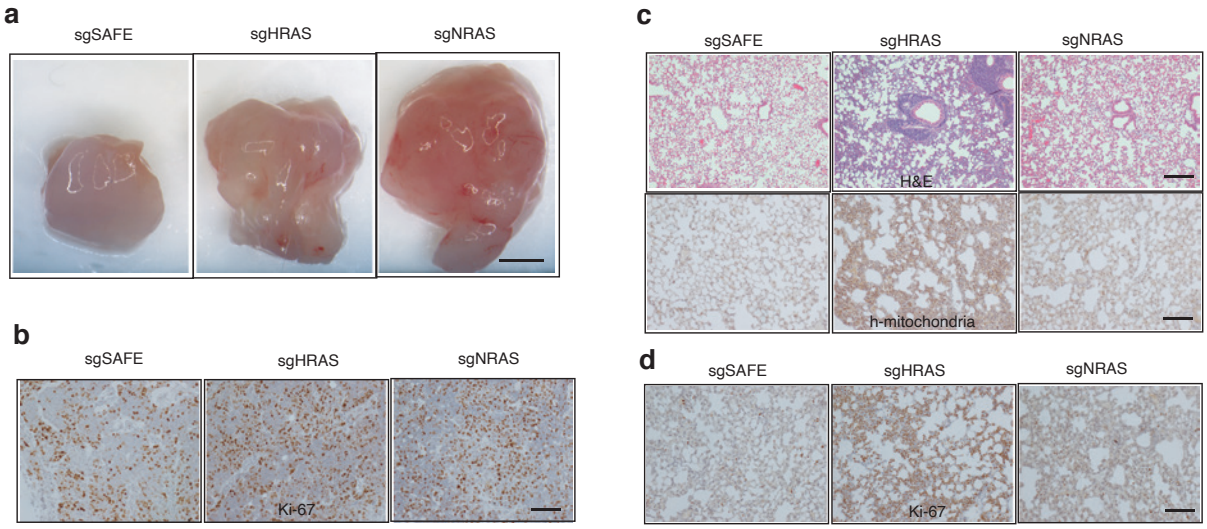

Supplemental Figure 5. Inactivation of wild type HRAS or NRAS increases H23 cell growth after transplantation.
a. Representative image of subcutaneous tumor size four weeks after transplantation with H23 cells as indicated. Quantification was shown in Figure 3h. Scale bar: 2 mm
b. Representative image of Ki67 staining from subcutaneous tumor four weeks after transplantation with H23 cells as indicated. Quantification was shown in Figure 3i. Scale bar: 100 µm
c. Representative image of HE (upper) and human mitochondria (lower) staining from lung tumor four weeks after intravenous transplantation with H23 cells as indicated. Quantification was shown in Figure 3j. Scale bar: 200 µm
d. Representative image of Ki67 staining from lung tumor four weeks after intravenous transplantation with H23 cells as indicated. Quantification was shown in Figure 3k. Scale bar: 200 µm

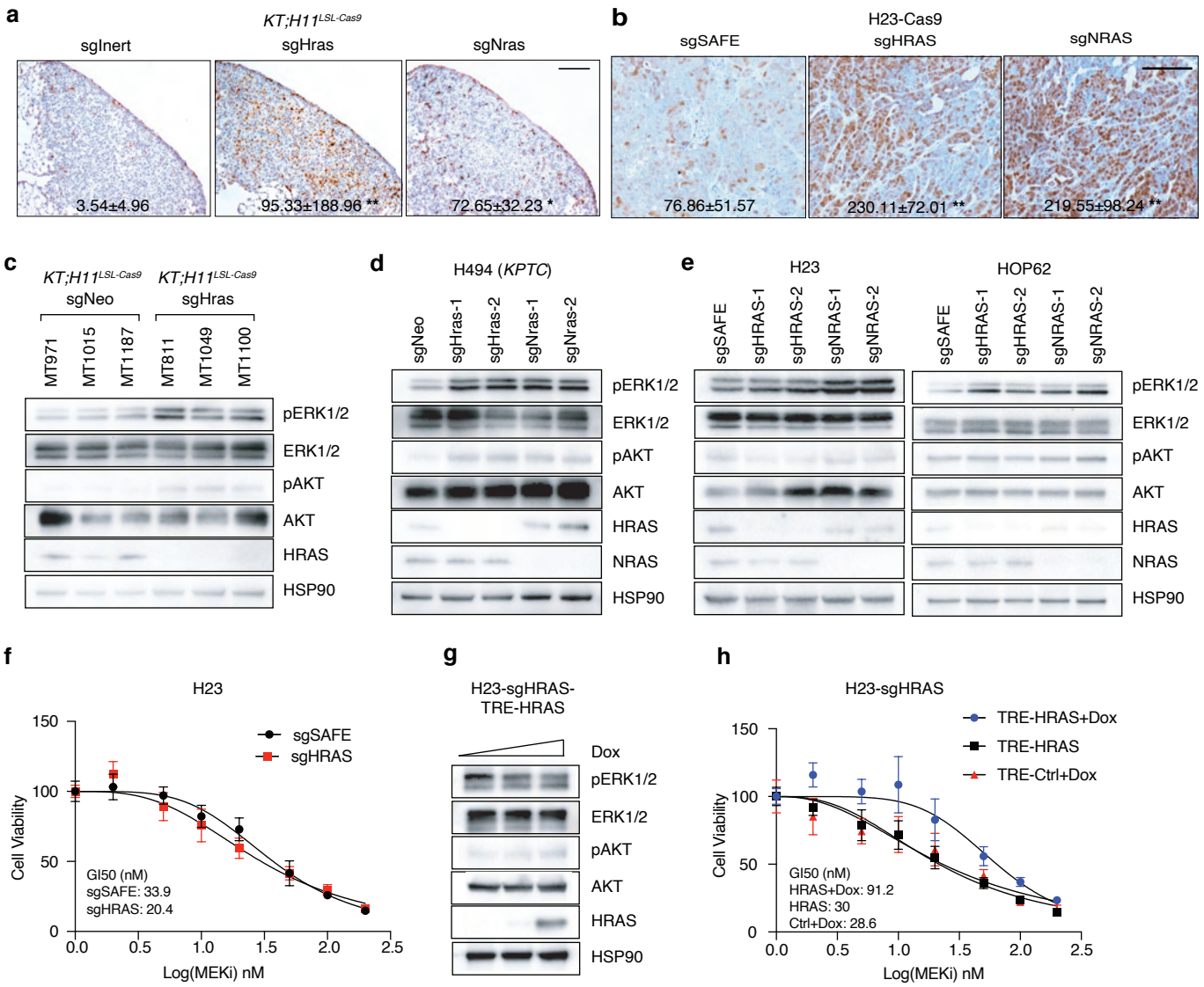

Figure 4. Wildtype RAS paralogs finetune RAS signaling

a. Representative image of pERK staining in KTC mice with tumors initiated with Lenti-sgRNA/Cre vectors as indicated. Quantification of pERK^{pos} cells per tumor was shown as Mean±SD of 20 tumors. *: $p<0.05$; **: $p<0.01$; Scale bar: 100 µm

b. Representative image of pERK staining in subcutaneous tumor transplantated with H23 cells as indicated. Quantification of pERK^{pos} cells per field was shown as Mean±SD of 20 fields. **: $p<0.01$; Scale bar: 100 µm

c. Western blot analysis of sorted cancer cells from KTC mice transduced with Lenti-sgRNA vectors as indicated. Each mice were transduced with 300k Lenti-sgRNA for 15 weeks. Multiple tumors from same mice (ear tag as indicated) were pooled for sorting and protein extraction.

d. Western blot analysis of cultured HC494 (KPTC) cells transduced with Lenti-sgRNA vectors as indicated. HC494 cells were transduced with lentiviral vector expressing indicated sgRNA and selected with puromycin to generate stable knockout cell lines. Wildtype cell (sgNeo) or HRAS- or NRAS-knockout cells (sgHras, sgNras) were cultured under limited serum (1%) for 2 days before protein extraction.

e. Western blot analysis of cultured H23 (left) and HOP62 (right) cells transduced with Lenti-sgRNA vectors as indicated. All human cells were transduced with lentiviral vector expressing indicated sgRNA and selected with puromycin to generate stable knockout cell lines. Wildtype cell (sgSAFE) or HRAS- or NRAS-knockout cells (sgHRAS, sgNRAS) were cultured under limited serum (1%) for 2 days before protein extraction.

f. Comparison of GI50 values to MEK inhibitors trametinib among wildtype and HRAS-null H23 cells under treatment of indicated dose of trametinib for four days. Cell number were measured via CCK8 assay and normalized to cells treated with vehicle. Each date point was shown as Mean±SD of 12 wells.

g. Western blot analysis of cultured HRAS-null H23 cells (H23-sgHRAS) re-expression HRAS (TRE-HRAS) under Doxycycline (Dox) treatment. HRAS-null H23 cells were generated from previous experiment as described in Figure 3a. HRAS-null H23 cells were re-transduced with lentiviral vector expressing TRE-HRAS at high MOI (>5) to generate stable HRAS re-expression cells (H23-sgHRAS-TRE-HRAS). To re-express HRAS, cells were treated with low dose (0, 1, and 2ng/ml) Dox and cultured under limited serum (1%) for 2 days before protein extraction.

h. Comparison of GI50 values to MEK inhibitors trametinib among HRAS-null H23 cells (H23-sgHRAS) re-expressing HRAS in presence (HRAS+Dox) or absence (HRAS) of Doxycycline plus indicated dose of trametinib for four days. Cell number were measured via CCK8 assay and normalized to cells treated with vehicle. Each date point was shown as Mean±SD of 12 wells.

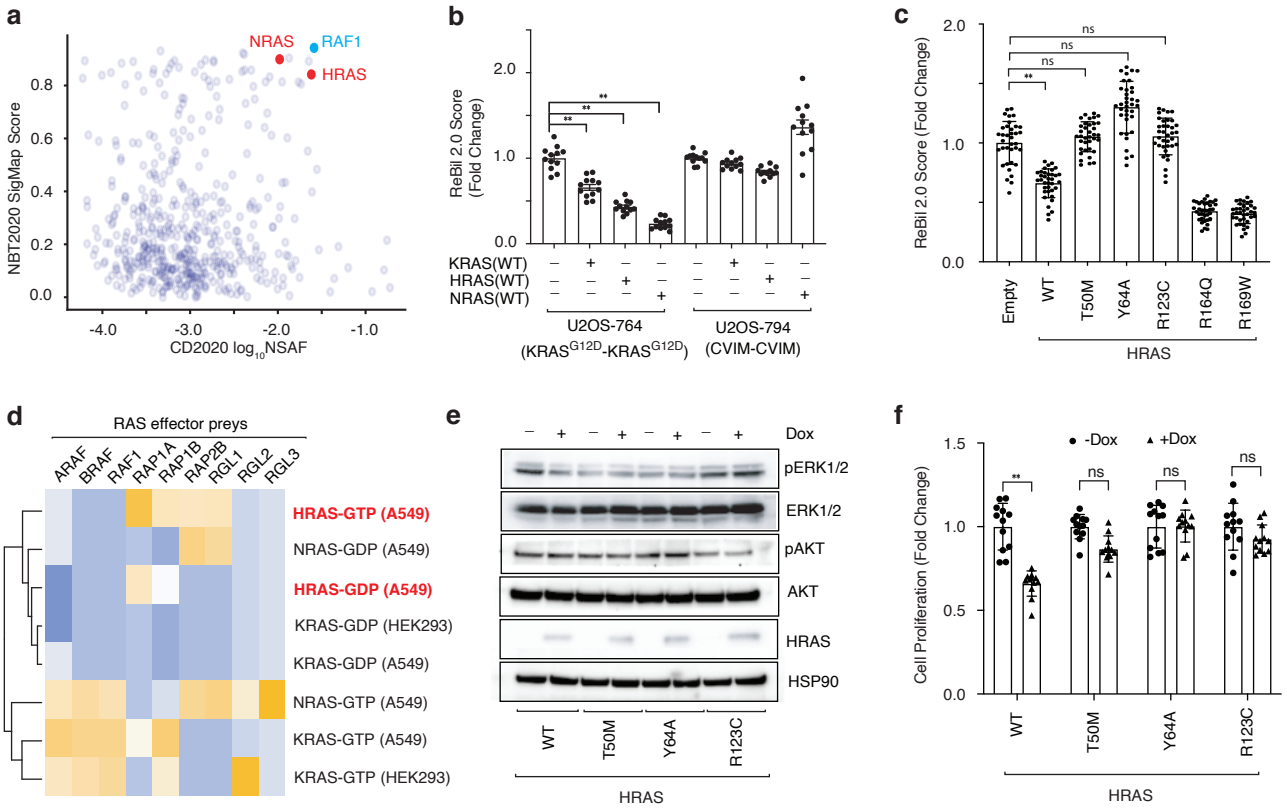

Figure 5. Wildtype RAS paralogs finetune RAS signaling through direct interaction with oncogenic KRAS.

a. HRAS and NRAS are shared KRAS interacting proteins in two protein-protein interaction datasets (Kelly, Kostyrko, Han et al. 2020; Broyde, Simpson, Murray et al. 2020). Shared KRAS-interaction proteins are shown as their $\log_{10}$NSAF and SigMap Score.

b. All three RAS proteins are able to disrupt $KRAS^{G12D}$-$KRAS^{G12D}$ interaction. U2OS-764 (nl-$KRAS^{G12D}$/cl-$KRAS^{G12D}$) or U2OS-794 (nl-CVIM/cl-CVIM) cells expressing KRAS, HRAS, or NRAS were cultured in limited serum (1%) under 100 ng/ml Doxycycline (Dox) for 24 hours. ReBiL2.0 assay were performed as previously described and detailed in Methods. Points are Mean±SD ReBiL2.0 score of 36 wells normalized to cells transduced with empty lentiviral vector. **: $p<0.01$,

c. $HRAS^{T50M}$ and $HRAS^{R123C}$ are novel dimerization deficient mutations. U2OS-764 (nl-$KRAS^{G12D}$/cl-$KRAS^{G12D}$) cells expressing wildtype or rare mutant HRAS were cultured in limited serum (1%) under 100 ng/ml Dox for 24 hours. Points are Mean±SD ReBiL2.0 score of 12 wells normalized to cells transduced with empty lentiviral vector. **: $p<0.01$; ns: not significant.

d. Clustermap of RAS effector prey proteins enriched in each experiment with the indicated baits in A549 cells (for K-, H-, or N-RAS) or HEK293 cells (for KRAS). Both GTP- and GDP-bond HRAS behave like GDP-bond KRAS in their RAS effector interactions.

e. Western blot analysis of cultured HRAS-null HOP62 cells (HOP62-Cas9-sgHRAS) re-expressing wildytype or dimerization deficient mutations (T50M, Y64A, or R123C) under Dox treatment. Cells were cultured under limited serum (1%) for 2 days before protein extraction. Re-expression of dimerization deficient mutations have no effects on ERK phosphrylation.

f. Cell proliferation of cultured HRAS-null HOP62 cells (HOP62-Cas9-sgHRAS) re-expressing wildytype or dimerization deficient mutations (T50M, Y64A, or R123C) under Dox treatment. Cells werer cultured in limited serum (1%) with or without Dox for 4 days. Cell viability was measured via CCK8 assay and normalized to cells treated with vehicle. Re-expression of dimerization deficient mutations have no effects on cell proliferation.

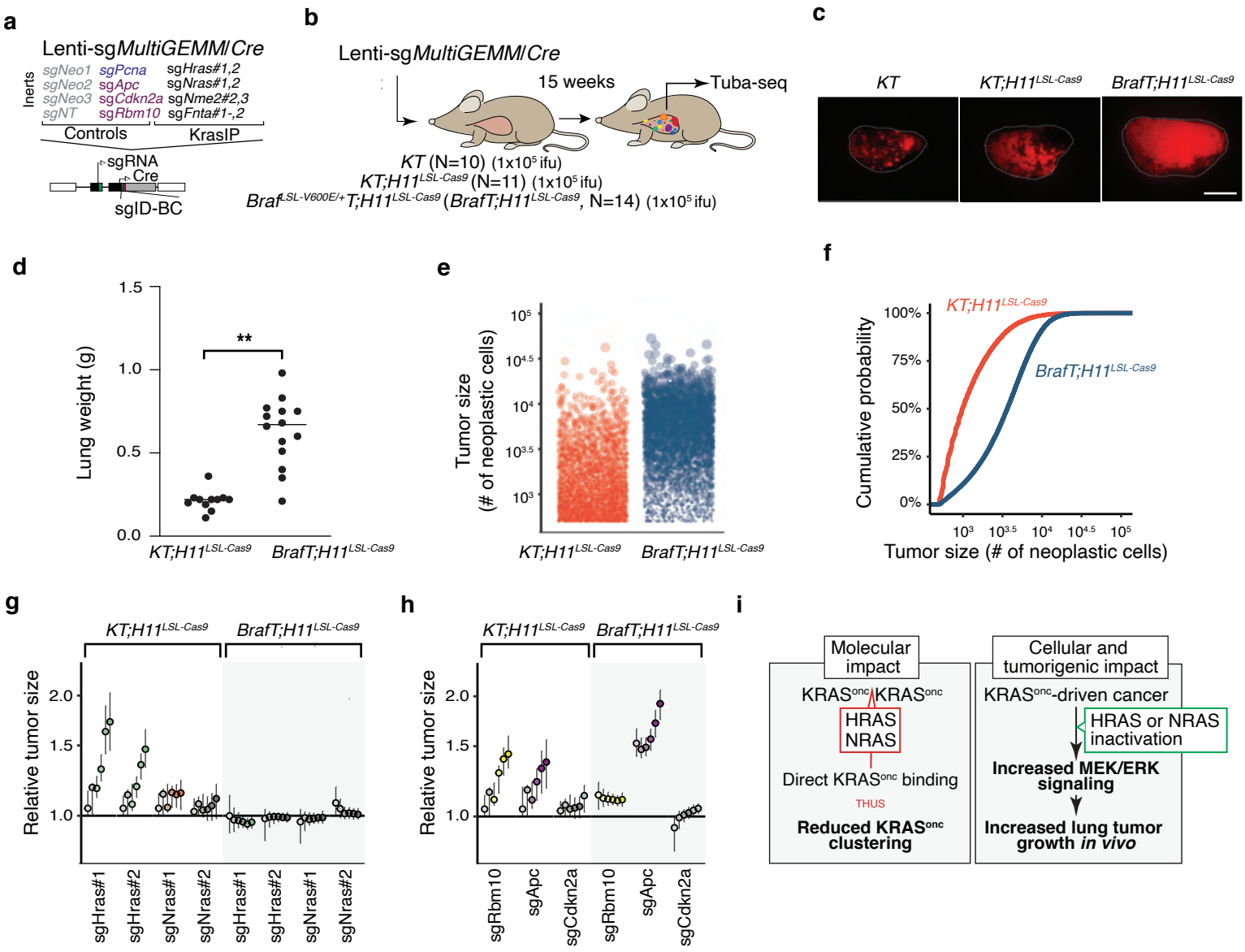

Figure 6. Paired screen in KRAS-driven and Braf-driven lung cancer models validates Hras and Nras as Kras-specific tumor suppressors.
a-b. Schematic of pairwise screen of tumor suppressive function in Kras- and Braf-driven lung cancer. A pool of barcoded Lenti-sgRNA/Cre vectors targeting top mediators of Kras-driven lung tumor growth (Lenti-sgMultiGEMM/Cre) was used to initiate tumors in cohorts of *KT;H11*$^{LSL\text{-}Cas9}$ and *Braf*$^{LSL\text{-}V600E/+}$*T;H11*$^{LSL\text{-}Cas9}$ (*BrafT;H11*$^{LSL\text{-}Cas9}$) mice. Each mediator of KRAS-driven tumor growth (*Hras*, *Nras*, *Nme2* and *Fnta*) was targeted by two sgRNAs (those with the largest effect size in the validation screen).The pool also included four Inert sgRNAs, as well as sgRNAs targeting *Apc*, *Cdkn2a*, and *Rbm10* as tumor suppressor controls (**a**). Tumors were initiated through intratracheal delivery of Lenti-sgMultiGEMM/Cre, and Tuba-seq was performed on each tumor-bearing lung 15 weeks after initiation, followed by analysis of sgID-BC sequencing data to characterize the effects of inactivating each gene (**b**).
c. Fluorescence images of representative lung lobes 15 weeks after tumor initiation. Scale bars = 5 mm. Lung lobes are outlined with a white dashed line.
d. Total lung weight in *KT;H11*$^{LSL\text{-}Cas9}$ and *BrafT;H11*$^{LSL\text{-}Cas9}$ mice 15 weeks after tumor initiation. Each dot is a mouse and mean value is indicated. **: $p<0.01$
e-f. Size distribution of sgInert tumors in *KT;H11*$^{LSL\text{-}Cas9}$ and *BrafT;H11*$^{LSL\text{-}Cas9}$ mice. In **e.**, each dot represents a tumor, and the area of each dot is proportional to the number of cancer cells in that tumor. To prevent overplotting a random sample of 1,000 tumors from each of five representative *KT;H11*$^{LSL\text{-}Cas9}$ and *BrafT;H11*$^{LSL\text{-}Cas9}$ mice are plotted. In **f.**, the empirical cumulative distribution function of tumor sizes across all *KT;H11*$^{LSL\text{-}Cas9}$ and *BrafT;H11*$^{LSL\text{-}Cas9}$ mice is plotted. Tumors >500 cells in size are shown.
g. Inactivation of *Hras* and *Nras* increases tumor size in *KT;H11*$^{LSL\text{-}Cas9}$ but not *BrafT;H11*$^{LSL\text{-}Cas9}$ models. Tumor sizes at indicated percentiles for each sgRNA relative to the size of sgInert-containing tumors at the corresponding percentiles in *KT;H11*$^{LSL\text{-}Cas9}$ (left, white background) and *BrafT;H11*$^{LSL\text{-}Cas9}$ (right, gray background) mice. Line at y=1 indicates no effect relative to sgInert. Error bars indicate 95% confidence intervals. Percentiles that are signficantly different from sgInert (two-sided FDR-adjusted $p < 0.05$) are in color. Confidence intervals and P-values were calculated by bootstrap resampling.
h.Comparison of the effects of inactivation of known tumor suppressors (*Rbm10*, *Apc*, and *Cdkn2a*) on tumor size in *KT;H11*$^{LSL\text{-}Cas9}$ and *BrafT;H11*$^{LSL\text{-}Cas9}$ models. Tumor sizes at indicated percentiles for each sgRNA relative to the size of sgInert-containing tumors at the corresponding percentiles in *KT;H11*$^{LSL\text{-}Cas9}$ (left, white background) and *BrafT;H11*$^{LSL\text{-}Cas9}$ (right, gray background) mice. Line at y=1 indicates no effect relative to sgInert. Error bars indicate 95% confidence intervals. Percentiles that are signficantly different from sgInert (two-sided FDR-adjusted $p < 0.05$) are in color. Confidence intervals and P-values were calculated by bootstrap resampling.
i. Schematic of wildtype RAS paralogs function as tumor suppressors in oncogenic KRAS signaling. Left panel, in oncogenic KRAS-driven lung cancer cells, wildtype RAS paralogs competetively interact with oncogenic KRAS and suppress oncogenic KRAS clustering. Right panel, inactivation of wildtype RAS allele, or "RAS paralog imbalance", hyper-activated oncogenic KRAS signaling and promotes lung cancer growth.

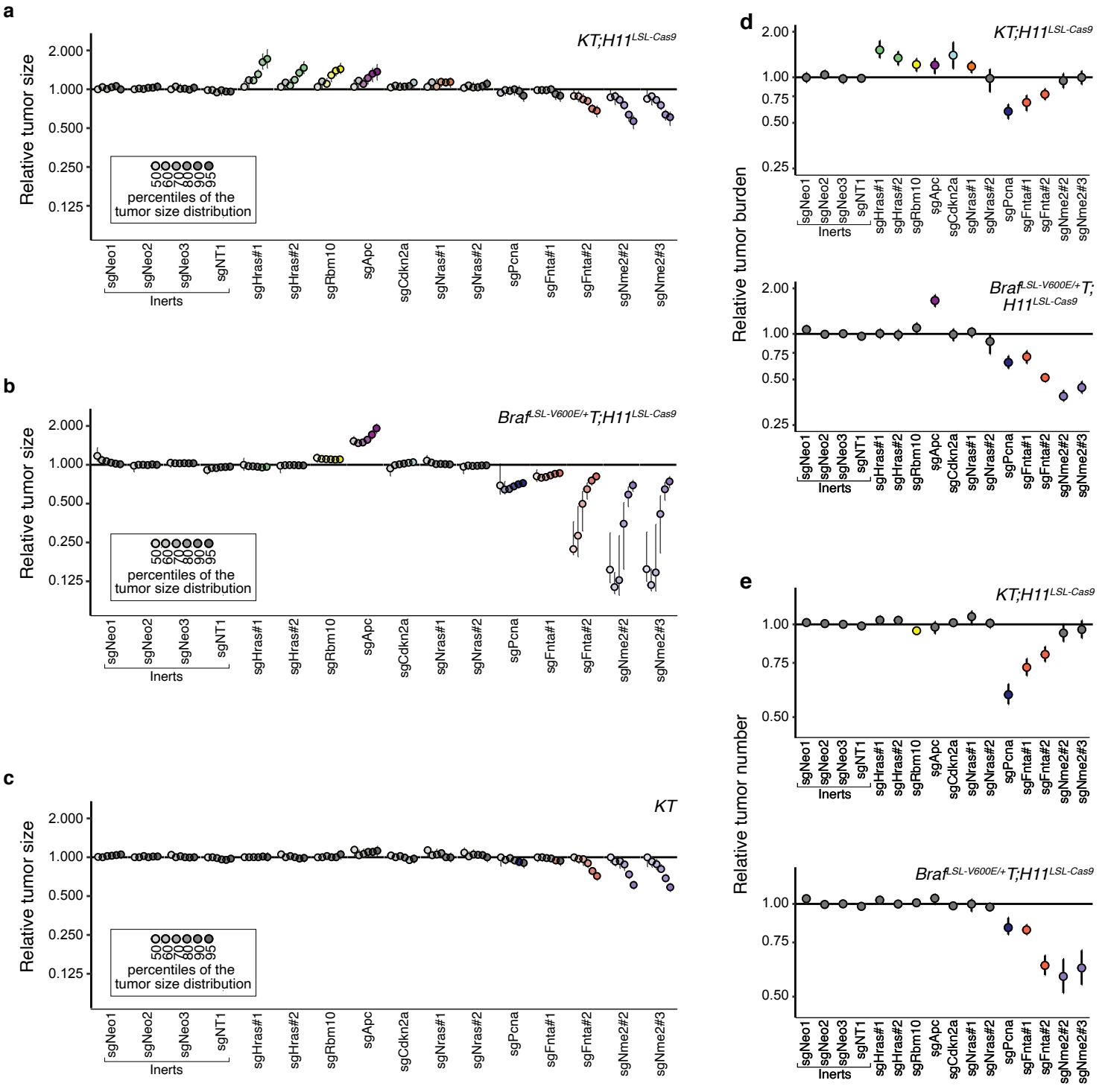

Supplemental Figure 6. Additional data from paired screen of Kras-interacting modulators of tumor growth in Kras-driven and Braf-driven lung cancer models

a-c. Tumor sizes at indicated percentiles for each sgRNA relative to the size of sgInert-containing tumors at the corresponding percentiles in *KTC* (**a**), *BrafTC* (**b**) and *KT* mice (**c**). Genes are ordered by 95th percentile tumor size in *KTC* mice, with sgInerts on the left. sgInerts are in gray, and line at y=1 indicates no effect relative to sgInert. Error bars indicate 95% confidence intervals. Percentiles that are signficantly different from sgInert (two-sided FDR-adjusted $p < 0.05$) are in color. Confidence intervals and P-values were calculated by bootstrap resampling.

d. The impact of each sgRNA on tumor burden relative to sgInerts in *KTC* (top) and *BrafTC* (bottom) mice, normalized to the corresponding statistic in *KT* mice to account for representation of each sgRNA in the viral pool. sgInerts are in gray and the line at y=1 indicates no effect. Error bars indicate 95% confidence intervals. Relative tumor burdens significantly different from sgInert (two-sided FDR-adjusted $p<0.05$) are in color. Confidence intervals and P-values were calculated by bootstrap resampling.

d. The impact of each sgRNA on tumor number relative to sgInerts in *KTC* (top) and *BrafTC* (bottom) mice, normalized to the corresponding statistic in *KT* mice to account for representation of each sgRNA in the viral pool. sgInerts are in gray and the line at y=1 indicates no effect. Error bars indicate 95% confidence intervals. Relative tumor numbers significantly different from sgInert (two-sided FDR-adjusted $p<0.05$) are in color. Confidence intervals and P-values were calculated by bootstrap resampling.